Available online at www.sciencedirect.com
SCIENCE DIRECT®
Comput. Methods Appl. Mech. Engrg. 193 (2004) 4979–5015
Computer methods in applied mechanics and engineering
www.elsevier.com/locate/cma

Local absorbing boundaries of elliptical shape for scalar waves

Loukas F. Kallivokas [a,b,*], Sanghoon Lee [a]

[a] Department of Civil Engineering, The University of Texas at Austin, 1 University Station C1748, Austin, TX 78712, USA
[b] Institute for Computational Engineering and Sciences, The University of Texas at Austin, USA

Received 28 January 2003; accepted 30 April 2004

Abstract

We discuss the performance of a family of local and weakly-non-local in space and time absorbing boundary conditions, prescribed on truncation boundaries of elliptical shape for the solution of the two-dimensional wave equation in both the time- and frequency-domains. The elliptical artificial boundaries are derived as particular cases of general convex boundaries for which the absorbing conditions have been developed. The conditions, via an operator-splitting scheme, are shown to lend themselves to easy incorporation in a variational form that, in turn, leads to a standard Galerkin finite element approach. The resulting wave absorbing finite elements are shown to preserve the sparsity and symmetry of standard finite element schemes in both the time- and frequency-domains. Numerical experiments for transient and time-harmonic cases attest to the computational savings realized when elongated scatterers are surrounded by elliptically-shaped boundaries, as opposed to the more commonly used circular truncation geometries.
© 2004 Elsevier B.V. All rights reserved.

Keywords: Absorbing; Artificial boundaries; Scalar waves; Elliptical shape; Time- and frequency-domains

1. Introduction

The need for the mathematical modeling and computational simulation of wave phenomena in unbounded media stems from a plethora of engineering problems that can be modeled mathematically as structures (or obstacles, scatterers, radiators, etc.) surrounded by an unbounded wave-supporting medium. In simulating numerically the propagating waves in an unbounded medium, the need for truncation boundaries that limit the infinite or semi-infinite extent of the physical domain to a finite computational one, typically arises when domain discretization methods provide the semi-discrete forms (e.g. FEM, FDM, FVM, etc.). On such an artificial boundary (the physical problem has no boundary), appropriate conditions need to be prescribed to allow for the safe passage of waves, with, ideally no, or at worse, minimal reflections, while simultaneously taking into account the behavior of the part of the physical domain, hereafter excluded from the computations.

* Corresponding author. Fax: +1-512-471-7259.
E-mail addresses: loukas@mail.utexas.edu (L.F. Kallivokas), sang@mail.utexas.edu (S. Lee).

0045-7825/$ - see front matter © 2004 Elsevier B.V. All rights reserved.
doi:10.1016/j.cma.2004.04.007

The central difficulty with domain discretization methods and the associated truncation boundaries stems from the need to satisfy an instantiation of the Sommerfeld radiation condition at the truncation boundary instead of at infinity. This condition is exact, and is typically referred to as the DtN map, for it relates the Dirichlet datum with the Neumann datum on the truncation boundary; it is however, non-local in both space and time. Local constructs of the DtN map that relax the spatial or the temporal non-locality, or both, are capable of reducing the computational cost associated with non-local conditions at the expense of accuracy.

By contrast, standard integral equation formulations, giving rise to boundary element methods, long dominant in frequency domain applications, satisfy a priori the radiation condition and thus bypass, by construction, the need for a truncation boundary. That is, the Green's functions present in the kernel of the integrals, satisfy automatically the radiation condition; however, classical integral equation formulations fall short due, at least, to: (a) non-locality of the formulations in both space and time, (b) difficulties in dealing with interior non-linearities, (c) lack of common time- and frequency-domain formulations, and (d) difficulties in dealing efficiently with domain sources. By far though, the primary difficulty with classical boundary element solutions in the frequency domain (Helmholtz) is due to the large size of the resulting algebraic equations: with increasing wavenumber, as in finite elements, the boundary surface discretization need also increase to resolve the underlying physics of wave propagation. By contrast though to the sparse systems resulting from finite element-type formulations, here the matrices are dense and often unsymmetric. In three dimensions, the solution of the resulting boundary element-based systems, may quickly become intractable in the large-frequency regime, even for modern hardware architectures. For cost comparisons, that shed a favorable light on finite elements versus boundary elements in the context of acoustics, see [1]. Therefore, despite the attractiveness of boundary element methods in reducing (in the absence of domain sources) the dimensionality of the problem by requiring only surface discretization, the shortcomings are too onerous. For the cited reasons, in this work, we favor a local treatment of the exact non-local truncation boundary condition, with an eye to the easy incorporation of the local absorbing conditions in finite element-based schemes.

2. Background

Whereas early treatments of truncation boundaries date back to the fifties [2], developments over the last decade allow for a loose classification of absorbing boundary conditions (ABCs) into local and non-local. In this context, non-locality implies the coupling of the observed response of one boundary point with the time histories of the response of every other point on the boundary, thus leading to conditions that, for the most part, can be thought as exact wave absorbers (exact DtN maps). By contrast, local conditions relax the spatial and temporal coupling to arrive at approximants of the exact truncation condition. The primary benefit of non-local conditions is accuracy at the expense of algorithmic simplicity and computational efficiency, whereas local conditions are typically computationally attractive at the expense of accuracy. A typical measure of computational attractiveness is the ease by which the conditions are coupled with the underlying domain discretization scheme of choice.

Recent renewed interest in devising local conditions of improved accuracy has also been fueled by the increased role that wave propagation simulations play in the characterization of the seismicity of a given geographic area. Furthermore, the computational power afforded by present day hardware architectures increasingly allows for the solution of otherwise intractable large-scale inverse problems aiming at the recovery of the skeletal properties of a wave-supporting medium. Such simulations are typically handled on distributed-memory parallel architectures, where minimizing processor-communication cost is of importance. In these cases, even if the implementation difficulties were to be overcome, the temporal and spatial coupling of non-local conditions typically dominate the communication patterns and tax heavily the total computational cost.

In the literature, several approaches to the construction of local ABCs have been followed (surveys on various absorbing boundaries, both early and recent, include the works by Kausel and Tassoulas [3], Wolf [4], Kausel [5], Givoli [6], and a recent fairly extensive and comprehensive review by Tsynkov [7]). Local constructs can be roughly classified in two categories: those based on rational approximations of the dispersion relation, and those based on asymptotic expansions of the far-field solution or the solution exterior to the computational domain.

Among the best-known hierarchies of local boundary conditions, representative of the first classification, are the sequences presented by Engquist and Majda [8,9] for the scalar wave equation. Starting with the dispersion relation that characterizes wave equations in dimensions higher than one, it is possible to show that the exact condition on the artificial boundary can be expressed via a pseudo-differential operator applied on the field variable(s). As mentioned, its non-local form (both spatial and temporal) makes it unsuitable or, at best, cumbersome for computations. Engquist and Majda's idea was to approximate the non-local operator by a local one; they approximated the irrational dispersion relation by rational Padé approximations, thus obtaining a sequence of absorbing boundary conditions, both in cartesian and polar coordinates in two dimensions.

A classical example of the second classification is the work of Bayliss and Turkel [10,11]; they developed a family of absorbing boundary conditions based on asymptotic expansions of the radial distance. Their conditions are applicable only to circular (in two dimensions) and spherical (in three dimensions) absorbing boundaries. Various implementations of the Bayliss and Turkel's conditions in the time- and frequency-domains have also been presented starting with the authors' comments in [12] (together with Gunzburger), where they considered the coupling of their first- and second-order conditions to finite elements.

Finite element implementations of the Bayliss' and Turkel's conditions have also appeared in works by Bossut, Decarpigny and co-workers [13,14], which, however, were limited to frequency-domain unsymmetric formulations. Later, Abboud and Pinsky [15] and Pinsky and Abboud [16,17] used the Bayliss and Turkel radiation conditions in conjunction with finite elements; the resulting formulations were either fourth-order symmetric or second-order unsymmetric when the second-order conditions were used.

To date the majority of the local ABC developments have been limited to circular or spherical truncation geometries. In practical applications, most notably those arising in underwater acoustics where the typical scatterer shape is of elongated geometry, circular or spherical artificial boundary geometries surrounding the scatterer typically result in large computational domains that are still costly to resolve. Thus, elliptically shaped, or, more generally, arbitrarily shaped convex geometries hold the promise for computational efficiency.

Non-local treatments of the exact DtN have also received considerable attention, and primarily so during recent years. The idea is to derive the exact boundary condition, or DtN map at the truncation boundary, based on a priori knowledge of the behavior of the solution in the domain exterior to a truncation boundary. The DtN is an exact condition, typically non-local in both time and space; the idea seems to have originated from the work of MacCamy and Marin [18]. Later, Keller and Givoli [20] and Givoli and Keller [19] presented DtN conditions based on circular and spherical absorbing boundaries in two and three dimensions, respectively. The method has been used predominantly for frequency-domain problems due to its non-local temporal character; finite element formulations involving the DtN have also appeared [21–23]. It is noteworthy that DtN approaches typically require a canonical geometry, usually circular or spherical; then it is possible to use the separation of variables apparatus to derive the associated harmonics in order to express the solution in the exterior domain. Such geometric restrictions however, may be onerous, primarily in three-dimensional time-dependent problems. We remark that recent developments on fast convolution evaluations (e.g. [24,25]) to an extent alleviate the temporal non-locality difficulty associated with DtN maps (for example, in [24], the cost is $O(N \log N)$, for N time-steps); the requirement for a circular or spherical boundary, however, remains.

Alternative treatments to the non-local DtN or to its local counterparts are offered by the, so-called, infinite elements, and the more recently developed PMLs (Perfectly Matched Layers).

The key concept in infinite elements is the representation of the decaying waves exterior to a truncation boundary by special elements extending in the radial direction and penetrating the infinite exterior domain. The idea seems to have originated from the pioneering work of Bettess [26,27]. Typically the truncation boundary is limited to a canonical geometry—circular, spherical, ellipsoidal, spheroidal, etc. (e.g. [28–30] for acoustic infinite elements); the elements can accommodate approximations of varying order of the exact decaying wave pattern along the radial direction. The majority of applications, however, are limited to the frequency-domain, with the notable exception of the work on wave envelope elements of Astley [31,32]. Wave envelope elements are particular cases of infinite elements; the interpolation functions used to approximate the decaying wave patterns are similar, or identical, to those used in infinite elements. However, the numerical implementation is cast in the context of a Petrov–Galerkin scheme where the test functions are complex conjugates of each other: this readily allows for the treatment of transient cases. It appears that these elements present the best challenge to local absorbing boundaries in terms of computational efficiency, but comparisons of relative performance characteristics have not yet appeared in the literature.

A recent method that strictly cannot fall under either the local or non-local classification pertains to the PML method. Bérenger [33] pioneered the idea for electromagnetic waves; it was later extended to the acoustics case by Qi and Geers [34]. To date there are two PML versions, a split and an unsplit version, where the splitting refers to the original idea [33] of splitting a wavefield into non-physical components. Accordingly, a buffer zone or layer is attached to the truncation boundary within which the waves are forced to die out by numerically controlling a damping coefficient. Despite the growing body of work and the early adoption of PMLs by the applied electromagnetics community, there still remain several open issues. Chief among them is the stability of the PMLs in transient cases: for example, in [35], it was shown that the split version (including the first acoustics implementation [34]) is ill-posed leading to exponential error growth for transient applications.

In the context of two-dimensional elliptically-shaped local boundaries we mention *ad hoc* (as opposed to systematic) developments [36–41] largely based on generalizations of the Bayliss–Turkel conditions to elliptical or general convex geometries without, however, the benefit of generalization to higher-order conditions, and the systematic works of Grote and Keller [42], Antoine et al. [43], Barry et al. [44], and Kallivokas et al. [45,47,48]. Finite element implementations of up to second-order conditions have recently appeared for elliptical and arbitrarily shaped geometries [49,50] for frequency-domain applications only, whereas comparisons of elliptical boundary developments up to 1996 have also been reported [51,52]. A comparison of these recently derived conditions with the ones presented herein is included in Section 3.2.2.

In this paper, we extend past work [45,47,48] that is based on a systematic development of ABCs for arbitrarily shaped convex artificial boundaries applicable to both the time- and frequency-domains by: (a) developing a third-order condition, (b) developing a new finite element based on the third-order condition fully characterized in terms of symmetric, time-invariant element mass, damping, and stiffness matrices that are tantamount to the effect of the artificial boundary (high-order "dampers"); and (c) presenting results for elliptically shaped boundaries that result in computational savings over their circular counterparts, using the higher-order conditions in both the time- and frequency-domains for scattering and radiation problems.

3. Mathematical formulation

To fix ideas we restrict the discussion to the exterior acoustics problem where the primary variable is the acoustic fluid pressure. However, a variety of other problems described by the scalar wave equation (e.g. the propagation of SH-waves) are identically treated (Fig. 1).

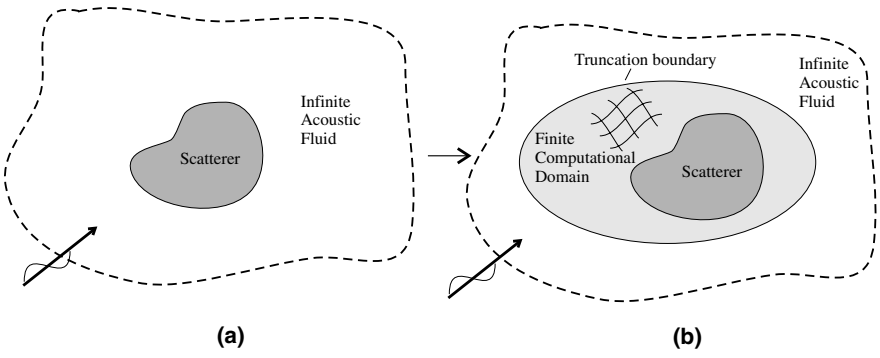

Fig. 1. (a) Scatterer surrounded by infinite fluid and (b) reduced model with finite computational region and truncation boundary in the presence of domain discretization.

3.1. The exterior problem

Let Γ be a closed surface with exterior $\Omega \subset \Re^2$ (Fig. 2a). Ω is occupied by a linear, inviscid, and compressible fluid. Without loss of generality, we consider the radiation problem in which Γ is subjected to a prescribed Neumann condition. Let us state the associated initial-and-boundary-value (IBVP) problem:

Find $p(\boldsymbol{x},t)$ such that

$$\ddot{p}(\boldsymbol{x},t) = c^2\Delta p(\boldsymbol{x},t), \quad \boldsymbol{x} \in \Omega, \quad t > 0, \tag{1a}$$

$$p_\nu(\boldsymbol{x},t) = f_{\mathrm{N}}(\boldsymbol{x},t), \quad \boldsymbol{x} \in \Gamma, \quad t > 0, \tag{1b}$$

$$\lim_{r\to\infty} \sqrt{r}\left(p_r + \frac{1}{c}\dot{p}\right) = 0 \quad \text{and} \tag{1c}$$

$$p(\boldsymbol{x},0) = 0, \quad \dot{p}(\boldsymbol{x},0) = 0, \quad \boldsymbol{x} \in \overline{\Omega}. \tag{1d}$$

In these equations p denotes pressure; $\boldsymbol{x}$ is the position vector, t is time; $\boldsymbol{\nu}$ is the outward unit normal on Γ; c is the velocity of wave propagation; Δ is the Laplace operator, and an overdot denotes derivative with respect to time. p_ν denotes the normal derivative of the pressure p, and f_{N} is the prescribed Neumann datum

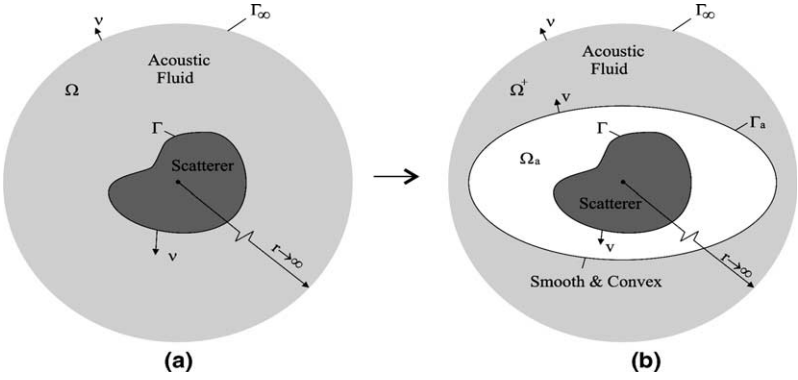

Fig. 2. (a) Model of scatterer surrounded by infinite acoustic fluid and (b) reduced model with finite fluid region Ω_a and absorbing boundary Γ_a.

on Γ. Condition (1c), in which r is radial distance and p_r the derivative of the pressure along the radial direction, is the Sommerfeld radiation condition. Condition (1d) indicates that the system is taken to be initially at rest.

The main difficulty associated with the solution of (1) is the need to ensure that the radiation condition (1c) is satisfied at infinity. To solve this problem using numerical methods based on the spatial discretization of the domain would require that, in the limit, one consider the complete, unbounded region Ω, a requirement that renders this approach infeasible. One way to make this problem manageable is to truncate the exterior region by introducing an artificial boundary Γ_a that contains Γ in its interior; this gives rise to a bounded subdomain Ω_a, as shown in Fig. 2b. In order for the solution p to coincide with that of the original problem within the truncated region Ω_a, it is necessary to specify a boundary condition on Γ_a that will ensure that the outgoing waves crossing Γ_a are undisturbed by the presence of this boundary. This boundary condition, which can be determined in terms of the actual solution p on Γ_a, as will be shown in Section 3.2.1, is of the form

$$p_v(\boldsymbol{x},t) = \mathscr{F}[p^t(\cdot,\cdot)](\boldsymbol{x}), \quad \boldsymbol{x} \in \Gamma_a, \tag{2}$$

in which $\boldsymbol{x}$ is position vector, the dots following p^t indicate dummy variables and $\mathscr{F}$ is an integral operator that depends on p^t, the time history of p, i.e.,

$$p^t(t) = p(t-\tau) \quad \forall \tau : 0 \leqslant \tau \leqslant t. \tag{3}$$

3.2. The absorbing boundary

3.2.1. Development

To determine the exact form of the operator $\mathscr{F}$ we consider the following problem associated with the original problem (1). The starting steps follow closely earlier developments [44,45] and are repeated here for completeness; departures and differences are noted as appropriate. We Laplace-transform (1a) with respect to time to obtain

$$s^2\hat{p}(\boldsymbol{x},s) = c^2\Delta\hat{p}(\boldsymbol{x},s), \quad \boldsymbol{x} \in \Omega, \tag{4}$$

where s is the Laplace-transform variable and a caret over a variable such as p denotes its Laplace transform. Suppose now that the surface Γ_a is smooth and convex, and let Ω^+ be the exterior of Γ_a (Fig. 2b). We focus on $\hat{p}$ in Ω^+ and formulate the following auxiliary Dirichlet problem in Ω^+ for an auxiliary field $\hat{P}$:

$$s^2\hat{P}(\boldsymbol{x},s;t) = c^2\Delta\hat{P}(\boldsymbol{x},s;t), \quad \boldsymbol{x} \in \Omega^+, \tag{5a}$$

with the boundary condition

$$\hat{P}(\boldsymbol{x},s;t) = p(\boldsymbol{x},t), \quad \boldsymbol{x} \in \Gamma_a. \tag{5b}$$

In (5) the use of a semicolon before t implies that t acts merely as a parameter. Then, by virtue of Duhamel's principle, one can show that (see Appendix A):

$$\hat{p}(\boldsymbol{x},s) = \int_0^\infty \mathrm{e}^{-st}\hat{P}(\boldsymbol{x},s;t)\mathrm{d}t, \quad \boldsymbol{x} \in \overline{\Omega}^+, \tag{6a}$$

and hence also

$$\hat{p}_v(\boldsymbol{x},s) = \int_0^\infty \mathrm{e}^{-st}\hat{P}_v(\boldsymbol{x},s;t)\mathrm{d}t, \quad \boldsymbol{x} \in \Gamma_a. \tag{6b}$$

Eq. (6a) together with Eqs. (5) ensure that the solution $\hat{p}$ in Ω^+ will coincide with the solution $\hat{p}$ in Ω from (4). From (5b) it can also be seen that the normal derivative $\hat{P}_v$ on Γ_a will be a linear functional of $p(\cdot,t)$ on Γ_a. Let us denote this dependency by

$$\hat{P}_v(\boldsymbol{x},s;t) = \widehat{\mathscr{F}}[p(\cdot,t)](\boldsymbol{x},s), \quad \boldsymbol{x}\in\Gamma_a, \tag{7a}$$

where $\widehat{\mathscr{F}}$ denotes a functional. By substituting (7a) into (6b) there results

$$\hat{p}_v(\boldsymbol{x},s) = \widehat{\mathscr{F}}[\hat{p}(\cdot,s)](\boldsymbol{x},s), \quad \boldsymbol{x}\in\Gamma_a. \tag{7b}$$

Then, translation of (7b) back to the time-domain yields

$$p_v(\boldsymbol{x},t) = \mathscr{F}[p^t(\cdot,\cdot)](\boldsymbol{x}), \quad \boldsymbol{x}\in\Gamma_a. \tag{7c}$$

Thus, in (7c) we recovered the form anticipated in (2). $\mathscr{F}$ denotes the functional (or DtN map) of the values of the pressure $p(\boldsymbol{y},\zeta)$ for $\boldsymbol{y}$ ranging over Γ_a and ζ from 0 to t. In other words, $\mathscr{F}$ merely expresses the fact that at any given instant t the motion at every point on the artificial boundary Γ_a is coupled with the time histories of all other points on Γ_a. The non-local character of the exact $\mathscr{F}$ makes it unsuitable for implementation in the context of domain methods. It is, thus, only natural to seek approximations to the exact $\mathscr{F}$ aiming primarily at reducing the temporal non-locality. It will be shown that this procedure also reduces automatically the spatial non-locality. To this end, we turn again to the auxiliary Dirichlet problem defined by (5) and introduce, borrowing from geometrical optics (p. 640 in [55]), an asymptotic expansion for $\widehat{P}$ of the form

$$\widehat{P}(\boldsymbol{x},s;t) \sim \mathrm{e}^{-(s/c)\chi(\boldsymbol{x})} \sum_{k=0}^{\infty} \left[\frac{c}{(s+\gamma(\boldsymbol{x}))a}\right]^k A^{(k)}(\boldsymbol{x},t), \quad \boldsymbol{x}\in\Omega^+, \tag{8a}$$

where a is a characteristic length of the absorbing boundary (e.g. in the case of a circular Γ_a, a is the radius), and $\chi(\boldsymbol{x})$ and $A^{(k)}(\boldsymbol{x},t)$ are as yet unknown functions. Without γ in (8a), the expansions are identical to the classical form provided in, e.g., [55]. However, as first noted in [44], and later also in, e.g., [57], higher-order absorbing boundary conditions resulting from (8a) without the γ correction are hopelessly unstable, that is, the use of the conditions will will lead to exponential error growth in time-dependent applications. Thus, γ in (8a) is introduced to alleviate the stability issue; in fact, $\gamma(\boldsymbol{x})$ is a, spatially variable, nonnegative parameter (see [45,47,48] for a detailed discussion). Through $\gamma(\boldsymbol{x})$ we attempt to ensure the dissipativity of the conditions for the continuous problem (prior to discretization). From a physical point of view, γ controls the amount of numerical damping introduced through the boundary Γ_a. The spatial variability of the control parameter γ is introduced here for the first time and it reflects the fact that the absorption characteristics depend also on the local geometry of the truncation boundary.

We require that the functions $\chi(\boldsymbol{x})$ and $A^{(k)}(\boldsymbol{x},t)$ satisfy the following conditions on Γ_a:

$$\chi(\boldsymbol{x}) = 0, \quad A^{(0)}(\boldsymbol{x},t) = p(\boldsymbol{x},t) \quad \text{and} \quad A^{(k)}(\boldsymbol{x},t) = 0 \quad \text{for } k \geqslant 1, \ \boldsymbol{x}\in\Gamma_a. \tag{8b}$$

Eqs. (8) ensure that $\widehat{P}$ is outgoing and that (5b) is satisfied automatically for any functions $\chi(\boldsymbol{x})$ and $A^{(k)}(\boldsymbol{x},t)$. Eq. (8a), by virtue of (8b), yields for $\widehat{P}_v$ on Γ_a

$$\widehat{P}_v(\boldsymbol{x},s;t) = -\frac{s}{c}\chi_v A^{(0)}(\boldsymbol{x},t) + \sum_{k=0}^{\infty} A_v^{(k)}(\boldsymbol{x},t)\left[\frac{c}{(s+\gamma(\boldsymbol{x}))a}\right]^k, \quad \boldsymbol{x}\in\Gamma_a. \tag{9a}$$

Substitution of (9a) in (6b) will therefore yield

$$\hat{p}_v(\boldsymbol{x},s) = -\frac{s}{c}\chi_v \widehat{A}^{(0)}(\boldsymbol{x},s) + \sum_{k=0}^{\infty} \widehat{A}_v^{(k)}(\boldsymbol{x},s)\left[\frac{c}{(s+\gamma(\boldsymbol{x}))a}\right]^k, \quad \boldsymbol{x}\in\Gamma_a. \tag{9b}$$

From (9b) and (6b) it can be seen that, once the unknown functions $\chi(\boldsymbol{x})$ and $A^{(k)}(\boldsymbol{x},t)$ are determined, an expression for the normal derivative p_v on Γ_a will be possible by translating (9b) back to time-domain. By introducing (8a) into (5a) and matching the coefficients of the various powers of the monomial $(s+\gamma)$ one obtains:

$$\sum_{k=0}^{\infty}\frac{c^k}{a^k}\left\{\left[\frac{1}{c^2}[|\nabla\chi|^2-1]A^{(k)}\right]\frac{1}{(s+\gamma)^{k-2}}+\left[\frac{1}{c^2}2\gamma[|\nabla\chi|^2-1]A^{(k)}+\frac{1}{c}[\Delta\chi A^{(k)}+2\nabla\chi\cdot\nabla A^{(k)}]\right]\frac{1}{(s+\gamma)^{k-1}}\right.$$
$$+\left[\frac{1}{c^2}\gamma^2[|\nabla\chi|^2-1]A^{(k)}+\frac{\gamma}{c}[\Delta\chi A^{(k)}+2\nabla\chi\cdot\nabla A^{(k)}]+\left[\Delta A^{(k)}+\frac{2k}{c}\nabla\chi\cdot\nabla\gamma A^{(k)}\right]\right]\frac{1}{(s+\gamma)^{k}}$$
$$\left.-\left[\frac{k}{c}\left[2\gamma\nabla\chi\cdot\nabla\gamma A^{(k)}+2\nabla\gamma\cdot\nabla A^{(k)}+\Delta\gamma A^{(k)}\right]\frac{1}{(s+\gamma)^{k+1}}\right]+\left[k(k+1)|\nabla\gamma|^2A^{(k)}\frac{1}{(s+\gamma)^{k+2}}\right]\right\}=0. \tag{10}$$

By setting to zero the coefficients of the various powers of the monomials $(s+\gamma)$ in (10), there result the following differential equations for the unknown functions $\chi(\boldsymbol{x})$ and $A^{(k)}(\boldsymbol{x},t)$, $(k\geqslant 0)$ with $\boldsymbol{x}\in\overline{\Omega}^+$:

$$|\nabla\chi|^2=1, \tag{11a}$$

$$2\nabla\chi\cdot\nabla A^{(0)}+\Delta\chi A^{(0)}=0, \tag{11b}$$

$$2\nabla\chi\cdot\nabla A^{(1)}+\Delta\chi A^{(1)}=a\Delta A^{(0)}, \tag{11c}$$

$$2\nabla\chi\cdot\nabla A^{(2)}+\Delta\chi A^{(2)}=a\left[\Delta A^{(1)}+\frac{2}{c}\nabla\chi\cdot\nabla\gamma A^{(1)}\right]+\frac{\gamma a}{c}[2\nabla\chi\cdot\nabla A^{(1)}+\Delta\chi A^{(1)}], \tag{11d}$$

$$\frac{c^{k+3}}{a^{k+3}}\frac{1}{c}[2\nabla\chi\cdot\nabla A^{(k+3)}+\Delta\chi A^{(k+3)}]+\frac{c^{k+1}}{a^{k+1}}\frac{1}{c}(k+1)\left[2\gamma\nabla\chi\cdot\nabla\gamma A^{(k+1)}+2\nabla\gamma\cdot\nabla A^{(k+1)}+\Delta\gamma A^{(k+1)}\right]$$
$$=\frac{\gamma}{c}\frac{c^{k+2}}{a^{k+2}}[2\nabla\chi\cdot\nabla A^{(k+2)}+\Delta\chi A^{(k+2)}]+\frac{c^{k+2}}{a^{k+2}}\left[\Delta A^{(k+2)}+\frac{2(k+2)}{c}\nabla\chi\cdot\nabla\gamma A^{(k+2)}\right]$$
$$+\frac{c^k}{a^k}k(k+1)|\nabla\gamma|^2A^{(k)},\quad k\geqslant 0. \tag{11e}$$

The differential equations (11a)–(11d), as well as the recursive set (11e) can be used to determine the unknown functions $\chi(\boldsymbol{x})$ and $A^{(k)}(\boldsymbol{x},t)$ for any k. To this end, we introduce a Fermi-type coordinate system in $\overline{\Omega}^+$ to aid in subsequent calculations (Fig. 3). Let Γ_a be described by the parametric representation $\boldsymbol{X}(\lambda)$, where $\boldsymbol{X}$ denotes the position vector on Γ_a and λ is an arc-length parameter. Then a new coordinate system is introduced in $\overline{\Omega}^+$ by the description

$$\boldsymbol{R}(\lambda,\xi)=\boldsymbol{X}(\lambda)+\xi\boldsymbol{v}(\lambda),\quad \xi\geqslant 0, \tag{12}$$

where $\boldsymbol{R}$ denotes position vector in Ω^+, ξ is a scalar and $\boldsymbol{v}$ is the outward normal to Γ_a (Fig. 3). With the proviso that Γ_a is convex and smooth, the new system is global in Ω^+. Notice that for $\xi=0$, (12) provides the parametric representation of Γ_a. By expressing the gradient, the Laplacian and the normal derivative in the new system (see appendix) one obtains for the normal derivatives of the unknown functions χ, $A^{(0)}$, $A^{(1)}$ and $A^{(2)}$

$$\chi_v(\boldsymbol{x})=\chi_\xi(\boldsymbol{x})=1,\quad \boldsymbol{x}\in\Gamma_a, \tag{13a}$$

$$A^{(0)}_v(\boldsymbol{x},t)=A^{(0)}_\xi(\boldsymbol{x},t)=\tfrac{1}{2}\kappa(\boldsymbol{x})A^{(0)}(\boldsymbol{x},t),\quad \boldsymbol{x}\in\Gamma_a, \tag{13b}$$

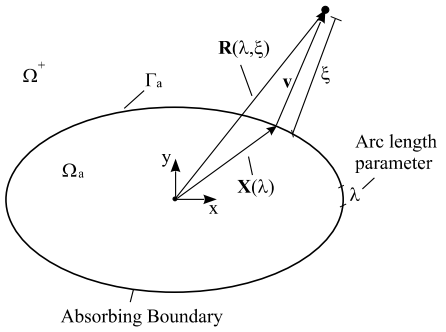

Fig. 3. A Fermi-type coordinate system characterized by the planar curve parameter λ and scalar distance metric ξ.

$$A_v^{(1)}(\boldsymbol{x},t) = A_\xi^{(1)}(\boldsymbol{x},t) = \tfrac{1}{2}a\left[A_{\lambda\lambda}^{(0)}(\boldsymbol{x},t) + \tfrac{1}{4}\kappa^2(\boldsymbol{x})A^{(0)}(\boldsymbol{x},t)\right], \quad \boldsymbol{x}\in\Gamma_a, \tag{13c}$$

$$\begin{aligned} A_v^{(2)}(\boldsymbol{x},t) = A_\xi^{(2)}(\boldsymbol{x},t) &= \frac{\gamma a^2}{2c}\left[A_{\lambda\lambda}^{(0)}(\boldsymbol{x},t) + \frac{1}{4}\kappa^2(\boldsymbol{x})A^{(0)}(\boldsymbol{x},t)\right] \\ &+ \frac{a^2}{2}\left[\kappa(\boldsymbol{x})A_{\lambda\lambda}^{(0)}(\boldsymbol{x},t) + \frac{1}{4}\kappa^3(\boldsymbol{x})A^{(0)}(\boldsymbol{x},t) + \frac{1}{4}\kappa_{\lambda\lambda}(\boldsymbol{x})A^{(0)}(\boldsymbol{x},t) + \kappa_\lambda(\boldsymbol{x})A_\lambda^{(0)}(\boldsymbol{x},t)\right], \quad \boldsymbol{x}\in\Gamma_a. \end{aligned} \tag{13d}$$

Letter subscripts above denote partial derivatives and κ denotes the curvature of Γ_a. [1] Next, by truncating the series in (8b) one can construct successive approximations to $\hat{p}_v$ and hence to the functional $\widehat{\mathscr{F}}[\hat{p}]$ in (7b). It can, therefore, be shown that by substituting the Laplace transforms of functions (13) into (9b), while taking into account (8b) and (7b), and keeping none, one, two or three terms from the series in (9b), the first four approximations for $\hat{p}_v$ on Γ_a are given as

$$\text{0th-order}: \hat{p}_v = \widehat{\mathscr{F}}_0[\hat{p}] = -\frac{s}{c}\hat{p}, \tag{14a}$$

$$\text{1st-order}: \hat{p}_v = \widehat{\mathscr{F}}_1[\hat{p}] = -\frac{s}{c}\hat{p} + \frac{1}{2}\kappa\hat{p}, \tag{14b}$$

$$\text{2nd-order}: \hat{p}_v = \widehat{\mathscr{F}}_2[\hat{p}] = -\frac{s}{c}\hat{p} + \frac{1}{2}\kappa\hat{p} + \frac{c}{2(s+\gamma)}\left(\hat{p}_{\lambda\lambda} + \frac{1}{4}\kappa^2\hat{p}\right), \tag{14c}$$

$$\begin{aligned} \text{3rd-order}: \hat{p}_v = \widehat{\mathscr{F}}_3[\hat{p}] &= -\frac{s}{c}\hat{p} + \frac{1}{2}\kappa\hat{p} + \frac{c}{2(s+\gamma)}\left(\hat{p}_{\lambda\lambda} + \frac{1}{4}\kappa^2\hat{p}\right) \\ &+ \frac{c^2}{2(s+\gamma)^2}\left[\kappa\hat{p}_{\lambda\lambda} + \kappa_\lambda\hat{p}_\lambda + \frac{1}{4}\kappa_{\lambda\lambda}\hat{p} + \frac{1}{4}\kappa^3\hat{p} + \frac{\gamma}{c}\left(\hat{p}_{\lambda\lambda} + \frac{1}{4}\kappa^2\hat{p}\right)\right], \end{aligned} \tag{14d}$$

where $\widehat{\mathscr{F}}_k$ $(k = 0,\ldots,3)$ denotes the approximate functional of kth order. Translation of (14) back to the time-domain yields:

$$\text{0th-order}: p_v = -\frac{1}{c}\dot{p}, \tag{15a}$$

[1] The closed convex planar curve Γ_a is oriented such that $\kappa(\boldsymbol{x}) < 0$, $\forall \boldsymbol{x}\in\Gamma_a$.

$$\text{1st-order}: p_v = -\frac{1}{c}\dot{p} + \frac{1}{2}\kappa p, \tag{15b}$$

$$\text{2nd-order}: \dot{p}_v + \gamma p_v = -\frac{1}{c}\ddot{p} + \left(\frac{1}{2}\kappa - \frac{\gamma}{c}\right)\dot{p} + \frac{1}{2}cp_{\lambda\lambda} + \left(\frac{1}{8}\kappa^2 c + \frac{1}{2}\kappa\gamma\right)p, \tag{15c}$$

$$\begin{aligned}\text{3rd-order}: \ddot{p}_v + 2\gamma\dot{p}_v + \gamma^2 p_v = {} & -\frac{1}{c}\dddot{p} + \left(\frac{1}{2}\kappa - \frac{2\gamma}{c}\right)\ddot{p} \\ & + \left(\frac{1}{8}\kappa^2 c + \kappa\gamma - \frac{\gamma^2}{c}\right)\dot{p} + \left(\frac{1}{2}\kappa\gamma^2 + \frac{1}{4}\kappa^2 c\gamma + \frac{1}{8}\kappa^3 c^2 + \frac{1}{8}\kappa_{\lambda\lambda}c^2\right)p \\ & + \left(\frac{1}{2}\kappa c^2 + \gamma c\right)p_{\lambda\lambda} + \frac{1}{2}\kappa_\lambda c^2 p_\lambda + \frac{1}{2}c\dot{p}_{\lambda\lambda}.\end{aligned} \tag{15d}$$

Remarks

(1) Conditions (15) are the desired approximations of the operator symbol in (2). Notice that all conditions are such that at the limit, as the truncation boundary approaches infinity, they reduce to the Sommerfeld radiation condition (1c): (14a) is obvious, whereas in (14b)–(14d) all curvature and tangential derivative terms vanish at the limit allowing only the first term to survive.

(2) Notice further that the lower-order conditions (15a) and (15b) are completely local in space and time, whereas the second- and third-order conditions (15c) and (15d) are only weakly non-local due to the presence of second-order tangential derivatives and higher-order time derivatives. It is possible to obtain even higher in order conditions following the systematic process outlined above (solutions to the recursive set (11) will lead to arbitrarily high-order conditions); however, as evidenced by (15), higher-order conditions will be characterized by increasing complexity and increasing loss of the local character attained by (15). Indeed, as can be seen from (15c) and (15d), the temporal locality is already affected; whereas (15a) and (15b) involve only the normal derivative of the pressure p_v, the last two introduce time derivatives of p_v as well. For conditions of order higher than the ones considered herein and despite the anticipated complexity it is possible to maintain the local character by introducing auxiliary functions on the boundary to replace the higher-order tangential derivatives; the process is systematic lending itself to implementation of higher-order conditions. For canonical geometries (circles and spheres) the auxiliary-function framework has been recently applied to the time-dependent two- and three-dimensional wave equations (see [56–59]). To address the mixed derivatives of the left-hand-side of (15), we follow a process similar to the auxiliary-function framework that also leads to the introduction of auxiliary variables on the truncation boundary. Our process is based on a decomposition or operator-splitting approach, first introduced in [45], and is addressed in detail in Section 3.2.3.

(3) Conditions (14a)–(14c) and their time-domain counterparts (15a)–(15c) derived here for a spatially variable γ turn out to be identical to conditions obtained before (e.g. [45,53,54]) for constant γ, whereas the third-order conditions (14d) and (15d) appear here for the first time.

(4) The introduction of the absorbing boundary Γ_a and the restriction of the infinite domain Ω to the finite domain Ω_a alters IBVP (1); accordingly, there results the following modified IBVP statement: Find $p(\boldsymbol{x}, t)$ such that

$$\ddot{p}(\boldsymbol{x}, t) = c^2 \Delta p(\boldsymbol{x}, t), \quad \boldsymbol{x} \in \Omega_a, \quad t > 0, \tag{16a}$$

$$p_v(\boldsymbol{x}, t) = f_{\mathrm{N}}(\boldsymbol{x}, t), \quad \boldsymbol{x} \in \Gamma, \quad t > 0, \tag{16b}$$

$$p_v(\boldsymbol{x},t) = \mathscr{F}_3[p^I](\boldsymbol{x}), \quad \boldsymbol{x}\in\Gamma_a, \quad t>0, \quad \text{and} \tag{16c}$$

$$p(\boldsymbol{x},0) = 0, \quad \dot{p}(\boldsymbol{x},0) = 0, \quad \boldsymbol{x}\in\overline{\Omega}_a, \tag{16d}$$

where, for example, the third-order condition has been used on Γ_a. We remark that the solution p to (16) should be such that its stability in time-domain applications be ensured, that is, we are interested in precluding exponential error growth, often associated with local approximate conditions such as (15). To study the stability of the solution to (16), we argue as follows (borrowing from similar arguments first cast in [44] and also used in [46] and [48]): let $\hat{p}$ be a solution of the Laplace-transformed IBVP (1), and let $\hat{q}$ be a solution of the Laplace-transformed IBVP (16). Then the error $\widehat{E} = \hat{p} - \hat{q}$ will satisfy

$$s^2\widehat{E}(\boldsymbol{x},s) = c^2\Delta\widehat{E}(\boldsymbol{x},s), \quad \boldsymbol{x}\in\Omega_a, \tag{17a}$$

$$\widehat{E}_v(\boldsymbol{x},s) = 0, \quad \boldsymbol{x}\in\Gamma, \tag{17b}$$

$$\widehat{E}_v(\boldsymbol{x},s) = \widehat{\mathscr{F}}_3[\widehat{E}](\boldsymbol{x},s) + \widehat{\Psi}(\boldsymbol{x},s), \quad \boldsymbol{x}\in\Gamma_a, \tag{17c}$$

where

$$\widehat{\Psi}(\boldsymbol{x},s) = \widehat{\mathscr{F}}[\hat{q}](\boldsymbol{x},s) - \widehat{\mathscr{F}}_3[\hat{q}](\boldsymbol{x},s), \quad \boldsymbol{x}\in\Gamma_a. \tag{17d}$$

$\widehat{\Psi}(\boldsymbol{x},s)$ for the above BVP (17) represents Neumann data on Γ_a. If problem (17) admits no non-zero solutions for $\Re e\, s > 0$ [2] (no poles in the right complex halfplane), then there will be no solutions for the error E of the form $E = \mathrm{e}^{\eta t}$, $\eta > 0$, and therefore no exponential error growth. The proof hinges on the definition of dissipativity for an operator such as the exact $\widehat{\mathscr{F}}$ and/or the approximant $\widehat{\mathscr{F}}_3$ given in [44]. In addition, therein the authors provided sufficient conditions for the dissipativity of the operators. We repeat them here (they were also used later in [48] for the three-dimensional case), using the third-order approximant $\widehat{\mathscr{F}}_3$ of (14d):

$$\Re e \int_{\Gamma_a} \widehat{\mathscr{F}}_3[\hat{p}](\boldsymbol{x},s)\bar{\hat{p}}(\boldsymbol{x},s)\mathrm{d}\Gamma_a < 0, \quad \text{for } s=\alpha>0, \tag{18a}$$

$$\Im m \int_{\Gamma_a} \widehat{\mathscr{F}}_3[\hat{p}](\boldsymbol{x},s)\bar{\hat{p}}(\boldsymbol{x},s)\mathrm{d}\Gamma_a \begin{matrix}<0\\>0\end{matrix} \quad \text{for } s=\alpha+\mathrm{i}\beta, \quad \alpha>0, \quad \begin{matrix}\beta>0,\\ \beta<0.\end{matrix} \tag{18b}$$

Substituting (14d) in (18a) yields

$$\begin{aligned} &-\frac{s}{c}\int_{\Gamma_a}|\hat{p}|^2\mathrm{d}\lambda + \int_{\Gamma_a}\left[\frac{1}{2}\kappa + \frac{\kappa^2 c}{8(s+\gamma)} + \frac{c^2\kappa_{\lambda\lambda} + c^2\kappa^3 + c\kappa^2\gamma}{8(s+\gamma)^2}\right]|\hat{p}|^2\mathrm{d}\lambda \\ &-\frac{c}{2}\int_{\Gamma_a}\left[\frac{1}{s+\gamma} + \frac{\kappa c+\gamma}{(s+\gamma)^2}\right]|\hat{p}_\lambda|^2\mathrm{d}\lambda + c\int_{\Gamma_a}\frac{\gamma_\lambda}{(s+\gamma)^3}[\kappa c+\gamma]\hat{p}_\lambda\bar{\hat{p}}\,\mathrm{d}\lambda < 0 \quad \forall s>0. \end{aligned} \tag{19}$$

Whereas it is possible through a judicious choice of γ to ascertain the sign of all but the last term in (19), the last term is cumbersome. To overcome, we set

$$\gamma(\boldsymbol{x}) = -c\kappa(\boldsymbol{x}). \tag{20}$$

[2] The case of $s=0$, that would lead to constant in time solutions, can be easily shown that it is not possible (see [44]).

With this choice, Eq. (20) forces the last term in (19) to vanish; there results

$$-\frac{s}{c}\int_{\Gamma_a}|\hat{p}|^2\mathrm{d}\lambda+\frac{1}{8}\int_{\Gamma_a}\frac{1}{(s-c\kappa)^2}\left[4\kappa s^2-7c\kappa^2 s+c^2(3\kappa^3+\kappa_{\lambda\lambda})\right]|\hat{p}|^2\mathrm{d}\lambda-\frac{c}{2}\int_{\Gamma_a}\frac{|\hat{p}_\lambda|^2}{s-c\kappa}\mathrm{d}\lambda<0\quad\forall s>0. \tag{21}$$

Clearly the first and third integral in (21) are negative (for $s>0$). The first and second terms of the second integral are also negative, and thus, to ensure that (21) is true, it suffices to show that $3\kappa^3+\kappa_{\lambda\lambda}<0$; the latter is true for all possible values of the aspect ratio of any ellipse (the proof is given in the appendix). Thus, condition (18a) is satisfied for the third-order approximant $\mathscr{F}_3$ of (14d). It is further trivial to show that the lower-order conditions (14a) and (14b) also satisfy (18a). Furthermore, in [44] it was shown that (18a) is satisfied for the second-order condition (14c), but (18b) is violated; (18b) is also violated by the third-order condition (14d) derived herein. However, numerically in, e.g., [45,53,54], no instability was observed using (14c) for any of the time-domain applications, even though the imaginary part of the dissipativity conditions (18b) was not satisfied. Similarly, in the three-dimensional counterpart of the second-order condition (see [48]), the real part of the dissipativity conditions (18a) was again satisfied, but the imaginary (18b) was violated with no observable error growth in numerical applications. Moreover, in [48] it was shown, via alternative means, that the second-order three-dimensional condition was stable for spherical boundaries. We remark that here too for both the second- and third-order absorbing conditions, the imaginary part of the dissipativity conditions (18b) is violated, yet no error-growth is observed numerically. To this date, we have not been able to provide a theoretical justification for relaxing (18b), and this remains an open issue. [3]

In summary, with (20), all conditions (14) satisfy the dissipativity condition (18a). Using (20), the second- and third-order conditions (14c) and (14d) reduce to:

$$\hat{p}_v=-\frac{s}{c}\hat{p}+\frac{1}{2}\kappa\hat{p}+\frac{c}{2(s-\kappa c)}\left(\hat{p}_{\lambda\lambda}+\frac{1}{4}\kappa^2\hat{p}\right), \tag{22a}$$

$$\hat{p}_v=-\frac{s}{c}\hat{p}+\frac{1}{2}\kappa\hat{p}+\frac{c}{2(s-\kappa c)}\left(\hat{p}_{\lambda\lambda}+\frac{1}{4}\kappa^2\hat{p}\right)+\frac{c^2}{2(s-\kappa c)^2}\left[\frac{1}{4}\kappa_{\lambda\lambda}\hat{p}+\kappa_\lambda\hat{p}_\lambda\right]. \tag{22b}$$

(5) As mentioned, in deriving conditions (14) and (15) we have assumed that γ varies spatially. This need not be the case: indeed, in, e.g. [53,54] numerical results in excellent agreement with exact solutions have been presented for conditions derived with the proviso of a constant γ and for circular boundaries. However, we expect, that the accuracy will be improved if γ were to reflect the spatial variability of the artificial boundary since, locally, γ controls the amount of damping introduced on the boundary. In Section 4 we provide numerical evidence that this is indeed the case.

3.2.2. Comparisons to other boundaries

We compare conditions (14) and their time-domain counterparts (15) to past and recent developments. A comparison with all developments pertaining to elliptically-shaped boundaries escapes the scope of this paper and thus the comparison here is limited to a few well-known sequences of absorbing boundaries on circular, elliptical, or arbitrarily convex boundaries. A detailed analysis of several conditions for elliptical or convex geometries up to 1996 can be found in the works of Meade et al. [51,52].

[3] In [44], it was shown that for (18a) to be satisfied using the second-order condition (14c) γ should be such that $\gamma\geqslant-\frac{c\kappa}{4}$; in [45,53,54] we showed that, for circular boundaries, the use of $\gamma=-c\kappa$ results in fewer reflections and is thus preferable for numerical calculations.

We consider first the well known Bayliss, Gunzburger, Turkel family of boundaries [10–12]. The authors proposed boundaries strictly for circular truncation geometries in the form

$$B_m p = 0, \quad \text{where} \quad B_m = \prod_{l=1}^{m} \left(\frac{1}{c}\frac{\partial}{\partial t} + \frac{\partial}{\partial r} + \frac{4l-3}{2r} \right). \tag{23}$$

The operator B_m annihilates the first m terms of the asymptotic expansion that is valid in the far-field, i.e., for large values of the radial distance r. Applying (23) for $m = 1$ and $m = 2$ yields (the $l = m$ term is the leftmost in the product in (23)):

$$m = 1: \; p_r = -\frac{1}{c}\dot{p} - \frac{1}{2a}p, \tag{24a}$$

$$m = 2: \; \dot{p}_r + \frac{c}{a}p_r = -\frac{1}{c}\ddot{p} - \frac{3}{2a}\dot{p} + \frac{c}{2a^2}p_{\theta\theta} - \frac{3c}{8a^2}p. \tag{24b}$$

Conditions (15b) and (15c) are identical to (24a) and (24b) respectively, provided that $\mathrm{d}\lambda = a\mathrm{d}\theta$ and $\kappa = -\frac{1}{a}$ are used in (15), and γ from (20) is taken as $\frac{c}{a}$, where a is the radius of the circular boundary and r, θ denote polar coordinates. Higher-order conditions using (23) depart from the ones derived herein.

In [8] Engquist and Majda were primarily concerned with straight-line boundaries. Using polar coordinates they provided the following first- and second-order conditions:

$$p_r = -\frac{1}{c}\dot{p} - \frac{1}{2a}p, \tag{25a}$$

$$\ddot{p}_r = -\frac{1}{c}\dddot{p} + \frac{1}{2a}\ddot{p} - \frac{c}{2a^2}\dot{p}_{\theta\theta} + \frac{c^2}{2a^3}p_{\theta\theta}. \tag{25b}$$

Clearly, (25a) coincides with (15b), while (25b) departs considerably from either (15c) or (15d) for any value of the control parameter γ.

Two-dimensional first- and second-order conditions also appeared in the work of Kriegsmann et al. [36]. Therein the conditions were first derived for a circular boundary and then, by an *ad hoc* reasoning, they were recast for a general convex geometry. The first-order condition is identical to (24a) (circular case) or to (15b) (general convex case). The second-order circular boundary condition coincides with the second-order (24b); in its general convex form the second-order condition in [36] can be written as

$$\dot{p}_v - \kappa c p_v = -\frac{1}{c}\ddot{p} + \frac{3}{2}\kappa\dot{p} + \frac{1}{2}cp_{\lambda\lambda} - \frac{3}{8}\kappa^2 cp. \tag{26}$$

Condition (26) coincides with (15c) provided $\gamma = -\kappa c$ (as in (20)). The authors in [36] used (26) as an on-surface boundary condition, i.e., they placed the absorbing boundary directly on the surface of the scatterer and obtained results for a number of TM (transverse magnetic) and TE (transverse electric) cases in the frequency-domain. We remark, that in [36] the conditions appeared only in the frequency-domain; we converted them here to the time-domain to ease the comparison.

In [42] Grote and Keller derived conditions for elliptically-shaped boundaries by using an approach similar to [10]. That is, they obtained the asymptotic expansions for the far-field solution valid for large values of the "radial" elliptical coordinate μ (r in the polar case) and constructed an operator product similar to (23) but cast in elliptical coordinates. Accordingly

$$B_m p = 0, \text{ where } B_m = \prod_{l=1}^{m} \left(\frac{1}{c}\frac{\partial}{\partial t} + \frac{1}{f\sinh\mu}\frac{\partial}{\partial \mu} + \frac{4l-3}{2f\cosh\mu} \right). \tag{27}$$

Using (27), the first-order condition, after appropriate coordinate transformations, can be written in the time-domain as

$$p_v = -\frac{f\sinh\mu}{l_1}\frac{1}{c}\dot{p} - \frac{1}{2}\frac{\tanh\mu}{l_1}p, \tag{28}$$

with $l_1 = f(\cosh^2\mu - \cos^2\phi)^{1/2}$, μ and ϕ denoting elliptical coordinates and f being the focal length of the ellipse. Though (28) can be shown to coincide with (24a) when the ellipse reduces to a circle, clearly (28) departs significantly from (15b): both coefficients on the right-hand side differ from the corresponding ones in (15b). Higher-order conditions are farther apart.

There are very few attempts to develop conditions in a systematic way for arbitrarily convex truncation geometries: chief among them is the work of Antoine at al., in [43] the authors developed three-dimensional conditions using the formal apparatus of pseudo-differential calculus. Whereas no details are given for the construction process by which two-dimensional conditions may arise, the authors in [43] provide a second-order two-dimensional condition by a suitable notational intervention to its three-dimensional counterpart. Using the notation employed herein, their second-order condition (Eq. (27) in [43]) reads

$$\hat{p}_v = -\frac{s}{c}\hat{p} + \frac{1}{2}\kappa\hat{p} + \frac{c}{2(s-\kappa c)}\left(\hat{p}_{\lambda\lambda} + \frac{1}{4}\kappa^2\hat{p}\right) + \frac{c^2}{2(s-\kappa c)^2}\kappa_\lambda\hat{p}_\lambda + \frac{c^2}{8s^2}\kappa_{\lambda\lambda}\hat{p}. \tag{29}$$

Notice that (29) differs from (22b), the third-order condition developed herein, in the last term only. Interestingly, (29) coincides with (22a) and the second-order (24b) for the case of a circle. We further remark that numerical results pertaining to (29) for time-harmonic problems have recently appeared in [49]. However, it appears that the authors in [49] have implemented, without justification or reference, a modified version of (29), where the last term in (29) has been dropped.

3.2.3. Condition decomposition—auxiliary variables

In order to discretize the problem within Ω_a using a Galerkin approach, we return to the strong statement (1), in order to recast it into a weak form. Notice, that the infinite domain Ω in (1) will now be replaced by the finite annular region Ω_a, as per (16). To construct the corresponding weak form we first multiply (16a) by a test function δp not subject to any boundary condition on Γ or Γ_a, integrate the result over Ω_a, and apply the divergence theorem to the term that contains the Laplacian operator. We then subtract the integral over Γ of (16b) multiplied by the restriction of δp to Γ. This process results in the classical form

$$\frac{1}{c^2}\int_{\Omega_a}\delta p\ddot{p}\,\mathrm{d}\Omega_a + \int_{\Omega_a}\nabla\delta p\cdot\nabla p\,\mathrm{d}\Omega_a - \int_{\Gamma_a}\delta p p_v\,\mathrm{d}\Gamma_a = -\int_{\Gamma} f_{\mathrm{N}}\delta p\,\mathrm{d}\Gamma. \tag{30}$$

Replacing p_v in the third integral in (30) by conditions (15a) or (15b) is trivial; on the other hand, the higher-order conditions (15c) and (15d), while expected to yield improved accuracy and computational economy due to the need for a smaller buffer region (Ω_a), cannot be readily implemented since they involve both the normal derivative of the pressure p_v as well as first and second time derivatives of p_v, respectively. Our aim is to make the conditions yield standard semi-discrete forms that are typical for interior problems. We show that this can be achieved via a wave- or operator-splitting approach realized through the introduction of additional degrees of freedom on the artificial boundary. We illustrate using the third-order condition (15d) or equivalently (22b); the procedure for condition (15c), for constant γ, can be found, e.g., in [53,54].

Let $q^{(1)}$, $q^{(2)}$, and $q^{(3)}$ denote auxiliary variables on Γ_a. Then, it is straightforward to show that the following set of four equations is tantamount to (22b):

$$-\hat{p}_v = \frac{s}{c}\hat{p} - \frac{1}{2}\kappa\hat{p} - \frac{c}{2\kappa}(\kappa\hat{q}^{(1)}_\lambda)_\lambda + \frac{c}{2\kappa}\kappa_\lambda\hat{q}^{(1)}_\lambda - \frac{c}{8}\kappa^2\hat{q}^{(2)} - \frac{c^2}{8}\kappa_{\lambda\lambda}\hat{q}^{(3)}, \tag{31a}$$

$$\hat{q}_{\lambda}^{(1)} = \frac{\hat{p}_{\lambda}}{s - \kappa c}, \tag{31b}$$

$$\hat{q}^{(2)} = \frac{\hat{p}}{s - \kappa c}, \tag{31c}$$

$$\hat{q}^{(3)} = \frac{\hat{p}}{(s - \kappa c)^2}. \tag{31d}$$

With the decomposition (31), incorporating the absorbing boundary condition (22b) in the variational statement is now substantially eased: multiply (31a) by δp, (31b) by $\delta q^{(1)}$, (31c) by $\delta q^{(2)}$, and (31d) by $\delta q^{(3)}$, where δp, $\delta q^{(1)}$, $\delta q^{(2)}$, and $\delta q^{(3)}$ are appropriate test functions, and integrate by parts. There results (after translation in the time-domain)

$$-\int_{\Gamma_a} \delta p p_v \, \mathrm{d}\Gamma_a = \frac{1}{c}\int_{\Gamma_a} \delta p \dot{p} \, \mathrm{d}\Gamma_a - \frac{1}{2}\int_{\Gamma_a} \kappa \delta p p \, \mathrm{d}\Gamma_a + \frac{c}{2}\int_{\Gamma_a} \delta p_{\lambda} q_{\lambda}^{(1)} \, \mathrm{d}\Gamma_a - \frac{c}{8}\int_{\Gamma_a} \kappa^2 \delta p q^{(2)} \, \mathrm{d}\Gamma_a - \frac{c^2}{8}\int_{\Gamma_a} \kappa_{\lambda\lambda} \delta p q^{(3)} \, \mathrm{d}\Gamma_a, \tag{32a}$$

$$\frac{c}{2}\int_{\Gamma_a} \delta q^{(1)} p_{\lambda} \, \mathrm{d}\Gamma_a - \frac{c}{2}\int_{\Gamma_a} \delta q^{(1)} \dot{q}_{\lambda}^{(1)} \, \mathrm{d}\Gamma_a + \frac{c^2}{2}\int_{\Gamma_a} \kappa \delta q^{(1)} q_{\lambda}^{(1)} \, \mathrm{d}\Gamma_a = 0, \tag{32b}$$

$$-\frac{c}{8}\int_{\Gamma_a} \kappa^2 \delta q^{(2)} p \, \mathrm{d}\Gamma_a + \frac{c}{8}\int_{\Gamma_a} \kappa^2 \delta q^{(2)} \dot{q}^{(2)} \, \mathrm{d}\Gamma_a - \frac{c^2}{8}\int_{\Gamma_a} \kappa^3 \delta q^{(2)} q^{(2)} \, \mathrm{d}\Gamma_a = 0, \tag{32c}$$

$$-\frac{c^2}{8}\int_{\Gamma_a} \kappa_{\lambda\lambda} \delta q^{(3)} p \, \mathrm{d}\Gamma_a + \frac{c^2}{8}\int_{\Gamma_a} \kappa_{\lambda\lambda} \delta q^{(3)} \ddot{q}^{(3)} \, \mathrm{d}\Gamma_a - \frac{c^3}{4}\int_{\Gamma_a} \kappa \kappa_{\lambda\lambda} \delta q^{(3)} \dot{q}^{(3)} \, \mathrm{d}\Gamma_a + \frac{c^4}{8}\int_{\Gamma_a} \kappa^2 \kappa_{\lambda\lambda} \delta q^{(3)} q^{(3)} \, \mathrm{d}\Gamma_a = 0. \tag{32d}$$

We remark that the presence of first-order derivatives in (31) or (32) increases the usual smoothness and continuity requirements on the truncation boundary Γ_a: we seek p and δp in $H^1(\Omega_a) \times H^{\frac{1}{2}}(\Gamma_a)$, but $q_{\lambda}^{(1)}, q^{(2)}, q^{(3)}, \delta q^{(1)}, \delta q^{(2)}, \delta q^{(3)}$ in $H^0(\Gamma_a)$. Eq. (29) can then be used to complete the weak-form formulation: the right-hand side of (32a) replaces the third term in (30), and (32b)–(32d) are added to the resultant functional. It is important to observe that with the decomposition (31), (30) will lead, upon spatial discretization, to a symmetric system of ordinary differential equations valid for both the frequency- and time-domains. In other words, the contributions from the absorbing boundary maintain both the symmetric structure of the interior problem and the sparsity of the associated system matrices.

A similar process can be followed for the second-order condition (22a); specifically, let

$$-\hat{p}_v = \frac{s}{c}\hat{p} - \frac{1}{2}\kappa\hat{p} - \frac{c}{2}\hat{q}_{\lambda\lambda}^{(1)} - \frac{c}{8}\kappa^2\hat{q}^{(2)}, \tag{33a}$$

$$\hat{q}_{\lambda\lambda}^{(1)} = \frac{\hat{p}_{\lambda\lambda}}{s - \kappa c}, \tag{33b}$$

$$\hat{q}^{(2)} = \frac{\hat{p}}{s - \kappa c}. \tag{33c}$$

Eqs. (33) are tantamount to (22a) and allow for the ready incorporation of the second-order (22a) (with variable γ) in the variational statement. Accordingly, multiply (33a) by δp, (33b) by $\delta q^{(1)}$, (30c) by $\delta q^{(2)}$, where δp, $\delta q^{(1)}$, and $\delta q^{(2)}$ are appropriate test functions, and integrate by parts (again we seek p and δp in $H^1(\Omega_a) \times H^{\frac{1}{2}}(\Gamma_a)$, and $q^{(1)}, \delta q^{(1)}$ in $H^{\frac{1}{2}}(\Gamma_a)$, $q^{(2)}, \delta q^{(2)}$ in $H^0(\Gamma_a)$. There results (in the time-domain)

$$-\int_{\Gamma_a} \delta p p_\nu \,\mathrm{d}\Gamma_a = \frac{1}{c}\int_{\Gamma_a} \delta p \dot{p}\,\mathrm{d}\Gamma_a - \frac{1}{2}\int_{\Gamma_a} \kappa \delta p p\,\mathrm{d}\Gamma_a + \frac{c}{2}\int_{\Gamma_a} \delta p_\lambda q_\lambda^{(1)}\,\mathrm{d}\Gamma_a - \frac{c}{8}\int_{\Gamma_a} \kappa^2 \delta p q^{(2)}\,\mathrm{d}\Gamma_a, \tag{34a}$$

$$\frac{c}{2}\int_{\Gamma_a} \delta q_\lambda^{(1)} p_\lambda \,\mathrm{d}\Gamma_a - \frac{c}{2}\int_{\Gamma_a} \delta q_\lambda^{(1)} \dot{q}_\lambda^{(1)}\,\mathrm{d}\Gamma_a + \frac{c^2}{2}\int_{\Gamma_a} (\kappa \delta q^{(1)})_{,\lambda} q_\lambda^{(1)}\,\mathrm{d}\Gamma_a = 0, \tag{34b}$$

$$-\frac{c}{8}\int_{\Gamma_a} \kappa^2 \delta q^{(2)} p\,\mathrm{d}\Gamma_a + \frac{c}{8}\int_{\Gamma_a} \kappa^2 \delta q^{(2)} \dot{q}^{(2)}\,\mathrm{d}\Gamma_a - \frac{c}{8}\int_{\Gamma_a} \kappa^3 \delta q^{(2)} q^{(2)}\,\mathrm{d}\Gamma_a = 0. \tag{34c}$$

Notice that, by contrast to the symmetric form (32) for the third-order condition (22b), the variational equations (34) are not symmetric. A symmetric scheme does not seem to exist to alleviate the problem in this case. However, in numerical experiments, we have found that if the derivative of the curvature term arising in (34b) were to be eliminated in favor of rendering (34) symmetric, there will be a marginal, if at all noticeable, effect to the error metrics. We have thus opted to drop the relevant term in favor of symmetry, and replace (34b) by

$$\frac{c}{2}\int_{\Gamma_a} \delta q_\lambda^{(1)} p_\lambda \,\mathrm{d}\Gamma_a - \frac{c}{2}\int_{\Gamma_a} \delta q_\lambda^{(1)} \dot{q}_\lambda^{(1)}\,\mathrm{d}\Gamma_a + \frac{c^2}{2}\int_{\Gamma_a} \kappa \delta q_\lambda^{(1)} q_\lambda^{(1)}\,\mathrm{d}\Gamma_a = 0. \tag{35}$$

3.3. Element matrices—new local absorbing finite elements

Standard finite element piecewise polynomial approximations (denoted here by $\boldsymbol{\psi}$) are used for approximating the geometry and for the spatial discretization of the pressure p in Ω_a and on Γ_a, and of the auxiliary variables on Γ_a. Introduce

$$p = \boldsymbol{\psi}^{\mathrm{T}}(\boldsymbol{x})\boldsymbol{p}, \quad \delta p = \boldsymbol{\delta p}^{\mathrm{T}}\boldsymbol{\psi}(\boldsymbol{x}), \tag{36a}$$

$$q_\lambda^{(1)} = \boldsymbol{\psi}^{\mathrm{T}}(\boldsymbol{x})\boldsymbol{q}^{(1)}, \quad \delta q^{(1)} = \boldsymbol{\delta q}^{(1)^{\mathrm{T}}}\boldsymbol{\psi}(\boldsymbol{x}), \tag{36b}$$

$$q^{(2)} = \boldsymbol{\psi}^{\mathrm{T}}(\boldsymbol{x})\boldsymbol{q}^{(2)}, \quad \delta q^{(2)} = \boldsymbol{\delta q}^{(2)^{\mathrm{T}}}\boldsymbol{\psi}(\boldsymbol{x}), \tag{36c}$$

$$q^{(3)} = \boldsymbol{\psi}^{\mathrm{T}}(\boldsymbol{x})\boldsymbol{q}^{(3)}, \quad \delta q^{(3)} = \boldsymbol{\delta q}^{(3)^{\mathrm{T}}}\boldsymbol{\psi}(\boldsymbol{x}). \tag{36d}$$

With the definitions (36) the element contributions of the absorbing boundary to the final semi-discrete form can be cast in terms of element mass $\boldsymbol{m}^a$, damping $\boldsymbol{c}^a$, and stiffness $\boldsymbol{k}^a$ element matrices, as it can be seen readily from (32), i.e., *Third-order absorbing element*

$$-\int_e \delta p^e p_\nu^e \,\mathrm{d}\Gamma_a^e = \begin{bmatrix} \boldsymbol{\delta p}_e \\ \boldsymbol{\delta q}_e^{(1)} \\ \boldsymbol{\delta q}_e^{(2)} \\ \boldsymbol{\delta q}_e^{(3)} \end{bmatrix}^{\mathrm{T}} \left\{ \boldsymbol{m}^a \begin{bmatrix} \ddot{\boldsymbol{p}}_e \\ \ddot{\boldsymbol{q}}_e^{(1)} \\ \ddot{\boldsymbol{q}}_e^{(2)} \\ \ddot{\boldsymbol{q}}_e^{(3)} \end{bmatrix} + \boldsymbol{c}^a \begin{bmatrix} \dot{\boldsymbol{p}}_e \\ \dot{\boldsymbol{q}}_e^{(1)} \\ \dot{\boldsymbol{q}}_e^{(2)} \\ \dot{\boldsymbol{q}}_e^{(3)} \end{bmatrix} + \boldsymbol{k}^a \begin{bmatrix} \boldsymbol{p}_e \\ \boldsymbol{q}_e^{(1)} \\ \boldsymbol{q}_e^{(2)} \\ \boldsymbol{q}_e^{(3)} \end{bmatrix} \right\}, \tag{37}$$

where the element matrices are given as

$$\boldsymbol{k}^a = \begin{bmatrix} -\frac{1}{2}\int_e \kappa\boldsymbol{\psi}\boldsymbol{\psi}^{\mathrm{T}} & \frac{c}{2}\int_e \boldsymbol{\psi}_\lambda\boldsymbol{\psi}^{\mathrm{T}} & -\frac{c}{8}\int_e \kappa^2\boldsymbol{\psi}\boldsymbol{\psi}^{\mathrm{T}} & -\frac{c^2}{8}\int_e \kappa_{\lambda\lambda}\boldsymbol{\psi}\boldsymbol{\psi}^{\mathrm{T}} \\ \frac{c}{2}\int_e \boldsymbol{\psi}\boldsymbol{\psi}_\lambda^{\mathrm{T}} & \frac{c^2}{2}\int_e \kappa\boldsymbol{\psi}\boldsymbol{\psi}^{\mathrm{T}} & 0 & 0 \\ -\frac{c}{8}\int_e \kappa^2\boldsymbol{\psi}\boldsymbol{\psi}^{\mathrm{T}} & 0 & -\frac{c^2}{8}\int_e \kappa^3\boldsymbol{\psi}\boldsymbol{\psi}^{\mathrm{T}} & 0 \\ -\frac{c^2}{8}\int_e \kappa_{\lambda\lambda}\boldsymbol{\psi}\boldsymbol{\psi}^{\mathrm{T}} & 0 & 0 & \frac{c^4}{8}\int_e \kappa^2\kappa_{\lambda\lambda}\boldsymbol{\psi}\boldsymbol{\psi}^{\mathrm{T}} \end{bmatrix}, \tag{38a}$$

$$\boldsymbol{c}^a = \begin{bmatrix} \frac{1}{c}\int_e \boldsymbol{\psi}\boldsymbol{\psi}^{\mathrm{T}} & 0 & 0 & 0 \\ 0 & -\frac{c}{2}\int_e \boldsymbol{\psi}\boldsymbol{\psi}^{\mathrm{T}} & 0 & 0 \\ 0 & 0 & \frac{c}{8}\int_e \kappa^2\boldsymbol{\psi}\boldsymbol{\psi}^{\mathrm{T}} & 0 \\ 0 & 0 & 0 & -\frac{c^3}{4}\int_e \kappa\kappa_{\lambda\lambda}\boldsymbol{\psi}\boldsymbol{\psi}^{\mathrm{T}} \end{bmatrix}, \tag{38b}$$

$$\boldsymbol{m}^a = \begin{bmatrix} 0 & 0 & 0 & 0 \\ 0 & 0 & 0 & 0 \\ 0 & 0 & 0 & 0 \\ 0 & 0 & 0 & \frac{c^2}{8}\int_e \kappa_{\lambda\lambda}\boldsymbol{\psi}\boldsymbol{\psi}^{\mathrm{T}} \end{bmatrix}. \tag{38c}$$

The subscript e denotes a line element on the truncation boundary Γ_a and the line differential ($\mathrm{d}\Gamma_a^e$) has been dropped throughout for brevity. Element matrices (38) define a new finite element which is capable of absorbing the waves that reach the artificial boundary while simulating the effect of the truncated infinite domain. The element defined by (38) is a surface-only element (Fig. 4); one need only mesh the finite region Ω_a and simply attach the absorbing element on the boundary Γ_a without any further discretization within the infinite exterior region. Notice that all matrices are frequency-independent and symmetric, thus readily allowing for applications in either the time- or frequency-domain, while maintaining the overall symmetry of the algebraic systems resulting from the discretization of the interior computational domain.

If the second-order condition (22a) were to be used, using the decomposition (33), the corresponding approximants are

$$p = \boldsymbol{\psi}^{\mathrm{T}}(\boldsymbol{x})\boldsymbol{p}, \quad \delta p = \boldsymbol{\delta p}^{\mathrm{T}}\boldsymbol{\psi}(\boldsymbol{x}), \tag{39a}$$

$$q^{(1)} = \boldsymbol{\psi}^{\mathrm{T}}(\boldsymbol{x})\boldsymbol{q}^{(1)}, \quad \delta q^{(1)} = \boldsymbol{\delta q}^{(1)^{\mathrm{T}}}\boldsymbol{\psi}(\boldsymbol{x}), \tag{39b}$$

$$q^{(2)} = \boldsymbol{\psi}^{\mathrm{T}}(\boldsymbol{x})\boldsymbol{q}^{(2)}, \quad \delta q^{(2)} = \boldsymbol{\delta q}^{(2)^{\mathrm{T}}}\boldsymbol{\psi}(\boldsymbol{x}), \tag{39c}$$

with *second-order absorbing element*

$$-\int_e \delta p^e p_v^e \,\mathrm{d}\Gamma_a^e = \begin{bmatrix} \boldsymbol{\delta p}_e \\ \boldsymbol{\delta q}_e^{(1)} \\ \boldsymbol{\delta q}_e^{(2)} \end{bmatrix}^{\mathrm{T}} \left\{ \boldsymbol{c}^a \begin{bmatrix} \dot{\boldsymbol{p}}_e \\ \dot{\boldsymbol{q}}_e^{(1)} \\ \dot{\boldsymbol{q}}_e^{(2)} \end{bmatrix} + \boldsymbol{k}^a \begin{bmatrix} \boldsymbol{p}_e \\ \boldsymbol{q}_e^{(1)} \\ \boldsymbol{q}_e^{(2)} \end{bmatrix} \right\}, \tag{40}$$

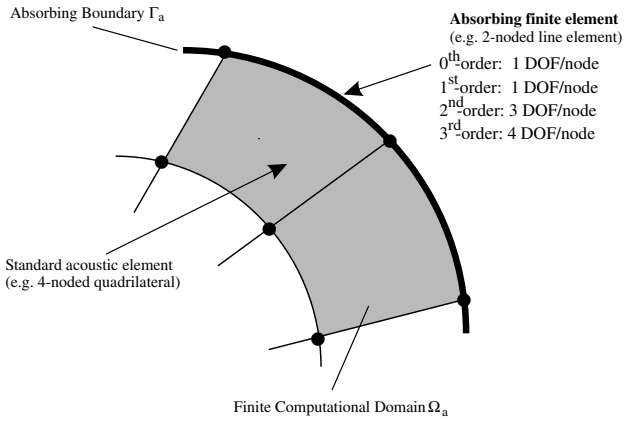

Fig. 4. Representation of the absorbing boundary element.

where the element matrices take the following form ([45,53,54]):

$$\boldsymbol{k}^a = \begin{bmatrix} -\frac{1}{2}\int_e \kappa \boldsymbol{\psi}\boldsymbol{\psi}^{\mathrm{T}} & \frac{c}{2}\int_e \boldsymbol{\psi}_\lambda \boldsymbol{\psi}_\lambda^{\mathrm{T}} & -\frac{c}{8}\int_e \kappa^2 \boldsymbol{\psi}\boldsymbol{\psi}^{\mathrm{T}} \\ \frac{c}{2}\int_e \boldsymbol{\psi}_\lambda \boldsymbol{\psi}_\lambda^{\mathrm{T}} & \frac{c^2}{2}\int_e \kappa \boldsymbol{\psi}_\lambda \boldsymbol{\psi}_\lambda^{\mathrm{T}} & 0 \\ -\frac{c}{8}\int_e \kappa^2 \boldsymbol{\psi}\boldsymbol{\psi}^{\mathrm{T}} & 0 & -\frac{c^2}{8}\int_e \kappa^3 \boldsymbol{\psi}\boldsymbol{\psi}^{\mathrm{T}} \end{bmatrix}, \tag{41a}$$

$$\boldsymbol{c}^a = \begin{bmatrix} \frac{1}{c}\int_e \boldsymbol{\psi}\boldsymbol{\psi}^{\mathrm{T}} & 0 & 0 \\ 0 & -\frac{c}{2}\int_e \boldsymbol{\psi}_\lambda \boldsymbol{\psi}_\lambda^{\mathrm{T}} & 0 \\ 0 & 0 & \frac{c}{8}\int_e \kappa^2 \boldsymbol{\psi}\boldsymbol{\psi}^{\mathrm{T}} \end{bmatrix}. \tag{41b}$$

We note that the element matrices (38) and (41) were obtained using the particular instances of the second- and third-order conditions derived in (22a) and (22b) respectively, for the value of the control parameter $\gamma = -c\kappa$ shown in (20). However, the symmetry and sparsity of the element matrices is not affected if constant values for γ were to be chosen. All that is required is that γ is such that the dissipativity criteria discussed in [44] and herein be satisfied.

Substitution of either (32) or (34) in the weak form (30), while taking into account the element semi-discrete forms (37) or (40) will result in the standard second-order semi-discrete matrix equation:

$$\boldsymbol{M}\ddot{\boldsymbol{p}}(t) + \boldsymbol{C}\dot{\boldsymbol{p}}(t) + \boldsymbol{K}\boldsymbol{p}(t) = \boldsymbol{F}(t), \tag{42}$$

where $\boldsymbol{p}$ includes both the interior nodal pressure values and the additional degrees-of-freedom values on the absorbing boundary. We remark that the system matrices are symmetric, but not positive-definite, due to the contributions of the absorbing boundary. Beyond the stability analysis discussed in Section 3.2.1 that ensures that the resulting (continuous) IBVP will not admit solutions that grow exponentially in time, we have not formally analyzed the spectral properties of the matrices involved in (42). However, we have used standard time-integration schemes to obtain time-domain solutions to (42) and have not observed instabilities.

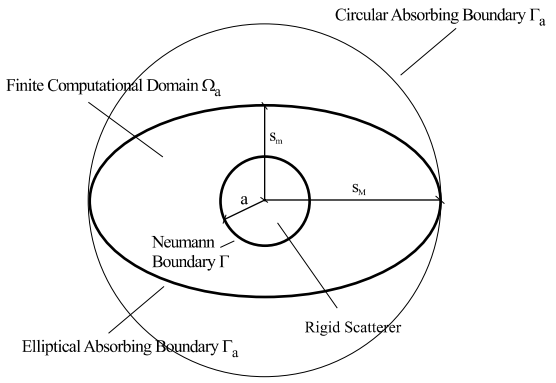

Fig. 5. Model of rigid scatterer and elliptical absorbing boundary.

4. Numerical results

Both the second- and third-order conditions were implemented on elliptically-shaped boundaries, as per the details of the preceding section. For the numerical implementation we have chosen bilinear 4-noded elements for the discretization of the finite domain Ω_a, and their traces on Γ_a (2-noded linear elements) as the absorbing boundary elements (Fig. 4). In all reported cases herein, the numerical results correspond to converged solutions. We remark that the theoretically expected convergence rates in, e.g., the $L_2(\Omega_a)$ norm remain unaffected by the use of the absorbing boundary conditions, at least for those cases for which an exact solution to the approximate problem was possible. [4]

Numerical experiments to assess the performance of the conditions and the associated discrete forms (elements (37)–(38) and (40)–(41)) were conducted for both radiation and scattering problems in the frequency- and time-domains. We report here on a subset of our numerical experiments focusing primarily on the second-order condition on elliptical boundaries. Results pertaining to the third-order condition are also included for the radiation problems.

4.1. Radiation problems

To assess the performance of the boundaries we consider first the radiation problem arising from prescribing an acceleration field on the surface of a circular scatterer (Fig. 5) of radius a; specifically, let

$$p_r = \rho A_0 \cos n\theta \mathrm{e}^{\mathrm{i}\omega t}, \tag{43}$$

where p_r denotes radial pressure derivative, ρ denotes the surrounding fluid's density, A_0 is the amplitude of the prescribed field, θ is polar angle, n denotes the order of the circumferential harmonic, and ω is the driving circular frequency. In this case, the exact solution for the radiated field in the domain exterior to the scatterer ($r \geqslant a$) is

$$p_{\mathrm{ex}}(r) = \frac{\rho A_0 a}{nH_n^{(2)}(ka) - kaH_{n+1}^{(2)}(ka)} H_n^{(2)}(kr)\cos n\theta, \tag{44}$$

[4] Such a case, for example, corresponds to circular boundaries surrounding a rigid circular scatterer; prescribing any order condition on the truncation boundary allows for an exact solution to the approximate problem—the problem defined over the finite domain Ω_a. This allowed us to compute the convergence rates.

Table 1
Total degrees-of-freedom per configuration—computational cost

Major semi-axis s_M/a	Minor semi-axis s_m/a	Semi-axes ratio $\eta = s_M/s_m$	Total DOF
3.0	3.0	1.0	68,064
3.0	2.5	1.2	57,158
3.0	2.0	1.5	41,496
3.0	1.5	2.0	29,114
6.0	6.0	1.0	292,972
6.0	5.0	1.2	239,820
6.0	4.0	1.5	186,176
6.0	3.0	2.0	140,056
6.0	1.5	4.0	65,354

where $k = \omega/c$ is the wavenumber, and $H_n^{(2)}$ denotes the second-kind Hankel function of order n. We surround the circular cavity with co-centric ellipses of various sizes and semi-axes ratios, and solve the boundary value problem in Ω_a using zero- to third-order conditions on Γ_a. We measure the relative error (for the response amplitude) using L_2 norms on the scatterer's boundary Γ (Fig. 5) as

$$E = \frac{\left[\int_\Gamma \|p_{ex} - p_{app}\|^2 \, d\Gamma\right]^{1/2}}{\left[\int_\Gamma \|p_{ex}\|^2 \, d\Gamma\right]^{1/2}} \times 100\%, \tag{45}$$

where p_{app} is the approximate solution obtained by solving (42) in the frequency-domain.

Denoting the major semi-axis with s_M, the minor semi-axis with s_m (Fig. 5), and the ratio of the two axes with $\eta = s_M/s_m$, Table 1 summarizes the computational cost associated with the various cases in terms of the total number of degrees-of-freedom. In all cases, the mesh density has been kept the same, resulting in a typical mesh size $h = 0.02a$. We consider frequencies between $ka = 0.5$ and $ka = 7$ (low and medium range); with these choices the smallest wavelength λ_ω is $0.9a$. Thus, for the highest frequency the mesh density corresponds roughly to 45 points per wavelength—more than enough to resolve locally the waves. [5] We observed no noteworthy change in the results by doubling the number of elements.

First, we are interested in establishing numerically the expected improved accuracy higher-order conditions are capable of attaining versus the lower-order conditions. To this end, Fig. 6 depicts the relative error (45) for conditions ranging from zero- to third-order for the considered frequency range and for values of the circumferential harmonic n between 0 and 7. The left column in Fig. 6 shows clearly the unacceptable error levels associated with the lower-order conditions. By contrast, both the second- and third-order conditions result in substantially lower errors and are thus preferable. The right column shows, in magnification, the curves corresponding to the second- and third-order conditions for the same set of parameters as in the left column: as it can be seen there is little, if anything, to be gained by the use of the third-order condition over the second-order condition, at least in the context of the particular radiation problem that we considered herein. Motivated by these observations, in the discussion of the remaining numerical experiments we focus exclusively on the performance of the second-order condition. We also remark that the worst error attained by the second-order condition (and also the third-order), as per Fig. 6, is about 4% for a frequency of $ka = 0.5$; moreover, as the frequency increases there is substantial error reduction. We attribute the higher errors associated with the lower frequencies to the fact that, by construction, our conditions are based on high-frequency expansions.

[5] Dispersion, as in all numerical simulations of propagating waves, remains an open issue; it is not addressed here and no schemes have been implemented to alleviate the dispersion error.

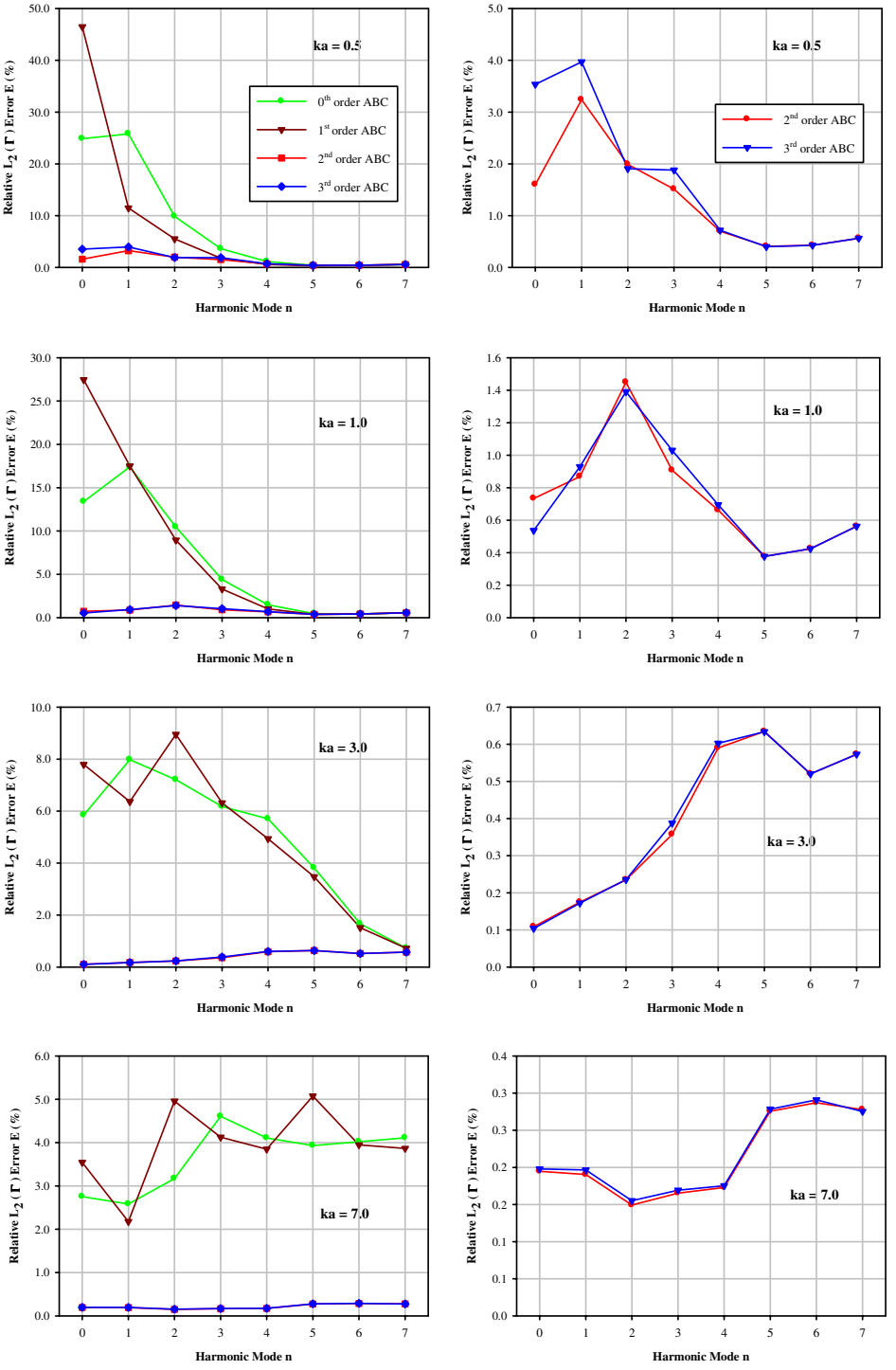

Fig. 6. Relative L_2 error E for an elliptical boundary with $s_{\mathrm{M}} = 3a$ and $\eta = 1.5$; various frequencies and harmonic modes; (left column): zeroth- to third-order conditions and (right column) rescaled details of right column showing second- and third-order conditions.

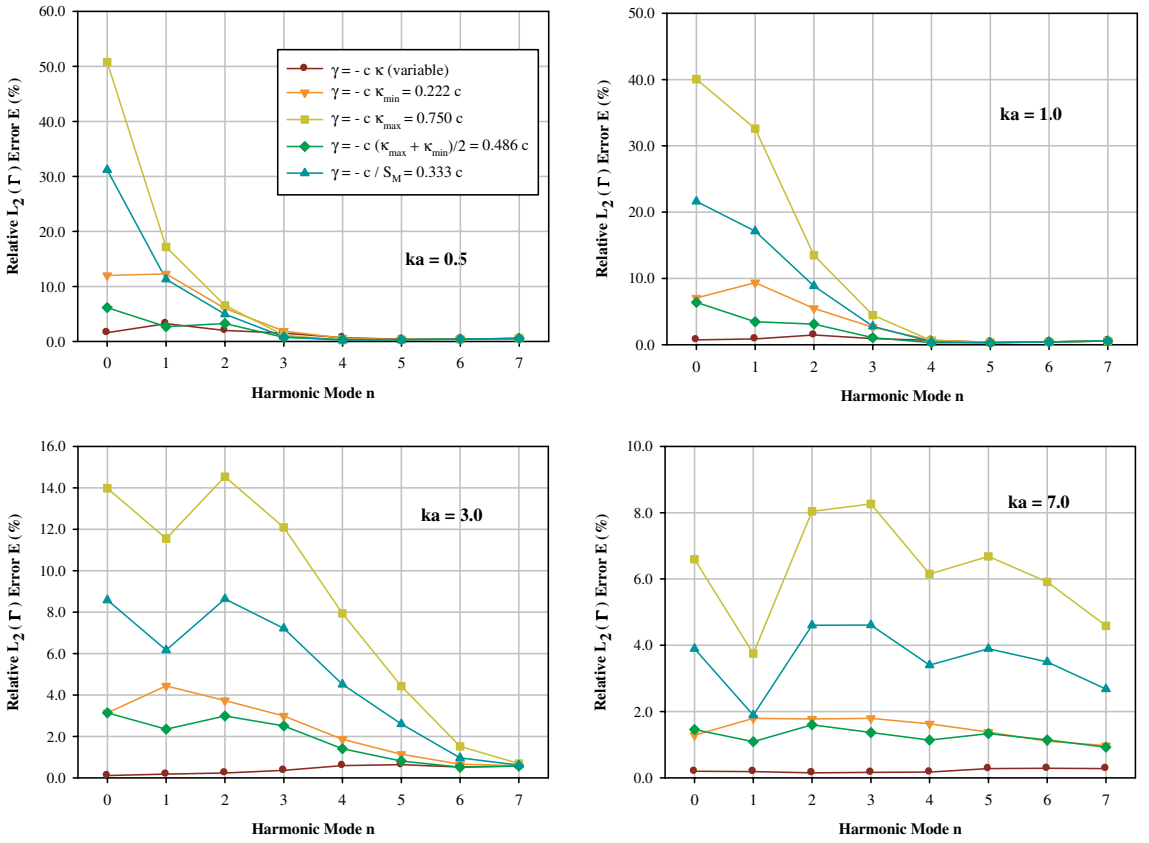

Fig. 7. Relative L_2 error E for an elliptical boundary with $s_M = 3a$ and $\eta = 1.5$; various γ parameter values, various frequencies and harmonic modes.

As mentioned in Section 3.2.3 we chose a spatially variable value for the stability parameter γ (20), partly motivated by physical intuition that the local absorption character of the boundary ought to reflect its geometry, and partly due to the stability analysis. However, a constant value for γ would also satisfy the stability criterion and is therefore a potential candidate. Fig. 7 provides numerical evidence that solutions to the same radiation problem and for various constant values of γ, and for the same range of frequencies and harmonic modes all underperform our variable γ choice (20). The relative errors shown in Fig. 7 were obtained using the second-order condition. [6] All subsequently reported results employ $\gamma = -c\kappa$ as per (20).

Figs. 8–11 summarize the errors for discrete frequencies ranging from $ka = 0.5$ to $ka = 7$ and for a harmonic mode sweep ranging from $n = 0$ to $n = 7$ corresponding to the first four cases reported in Table 1: that is, for ellipse semi-axes ratios ranging from 1 to 2, and for placement of the boundary at a maximum distance of 3a. Similarly, Figs. 12–16 depict the errors for the last five cases of Table 1, for ellipse semi-axes ratios ranging from 1 to 4, with $6a$ being the maximum distance at which the boundary is placed (we keep the same frequency and harmonic ranges).

As it can be seen from Figs. 8–15, in nearly all cases both elliptical and circular boundaries perform well. We observe, however, that at the low frequency and low harmonic regime: (a) the circular boundary for the

[6] For this condition, the stability criterion mandates that $\gamma \geqslant -c\frac{\kappa_{\max}}{4}$; all constant γ values shown in Fig. 7 satisfy the criterion.

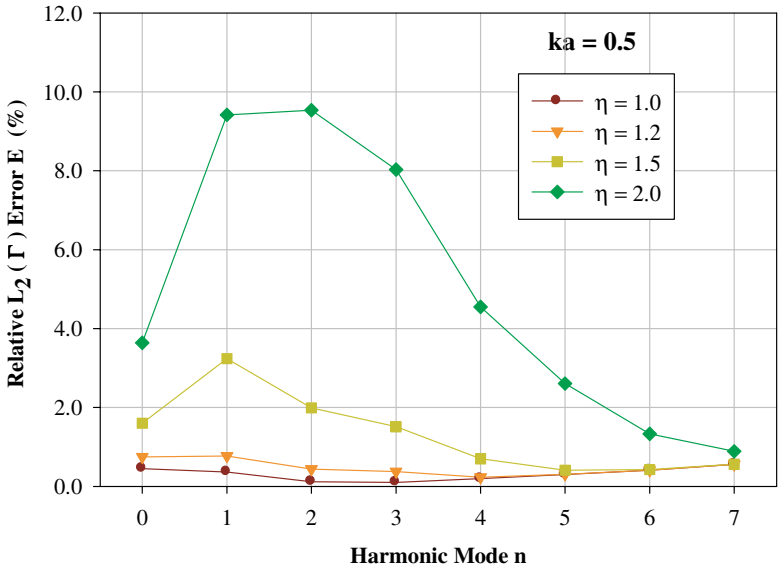

Fig. 8. Relative L_2 error E for elliptical ($s_M = 3a$) and circular boundaries; $ka = 0.5$; various harmonic modes.

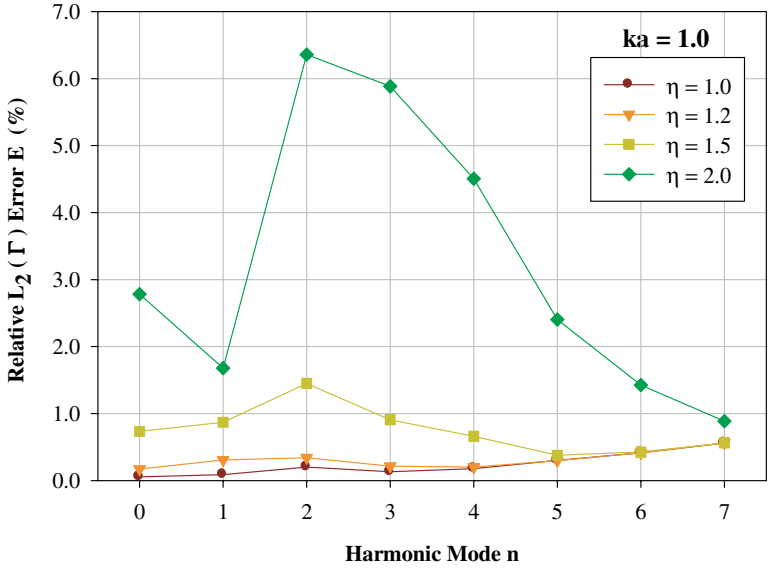

Fig. 9. Relative L_2 error E for elliptical ($s_M = 3a$) and circular boundaries; $ka = 1.0$; various harmonic modes.

same mesh density performs better than the elliptical ones (Fig. 8), though at increased computational cost (Table 1), and (b) the errors are greater at low frequencies as the semi-axes ratio η increases, i.e., as the ellipse departs increasingly from a circular configuration. For example, for $\eta = 4$ and $ka = 0.5$, the errors are clearly unacceptable (Fig. 12). We site two reasons: first, in this case, the absorbing boundary, at its closest point to the scatterer, is at a distance of only 0.04 of the dominant wavelength from the scatterer.

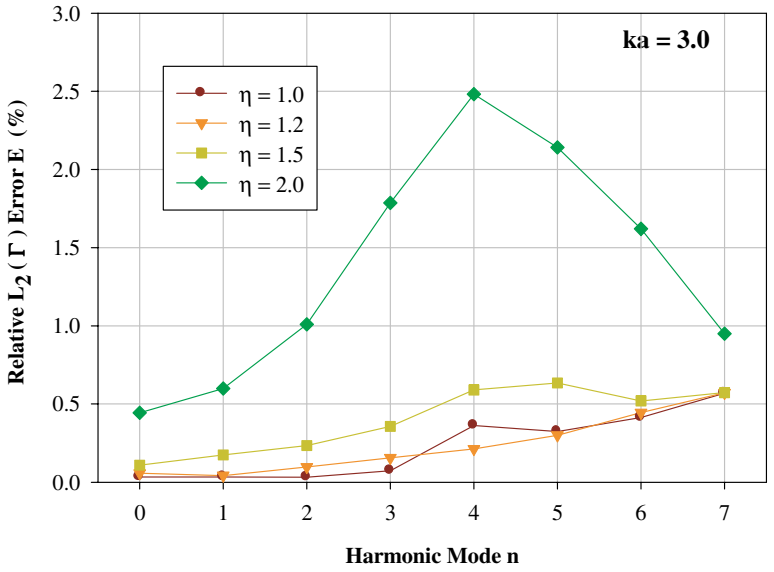

Fig. 10. Relative L_2 error E for elliptical ($s_M = 3a$) and circular boundaries; $ka = 3.0$; various harmonic modes.

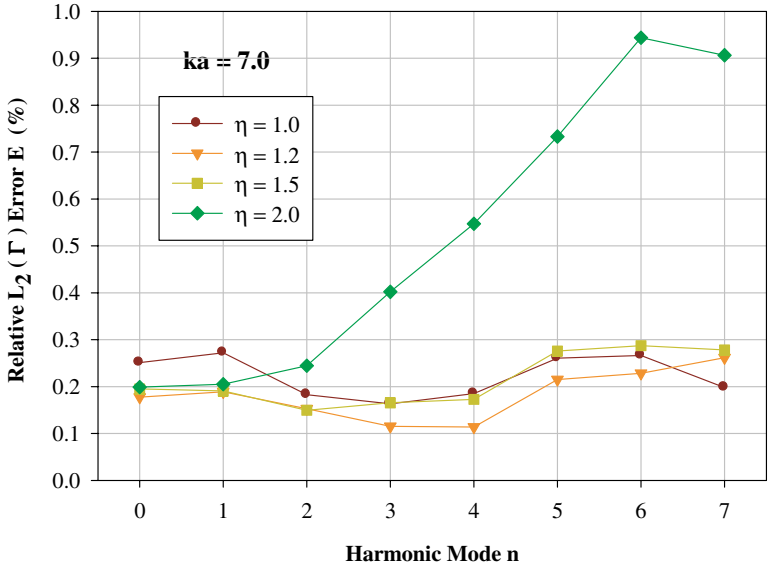

Fig. 11. Relative L_2 error E for elliptical ($s_M = 3a$) and circular boundaries; $ka = 7.0$; various harmonic modes.

At such small distances, or equivalently, for such small dimensionless wavenumbers, and irrespective of the mesh resolution, the conditions are defeated; again, this is so by construction. We recall that we used high-frequency expansions to construct the conditions and thus expect the boundaries to perform well at the medium to high frequency range, as indeed is shown to be the case. Our observations here are in tandem with earlier experiments with very-low frequencies in the frequency-domain and with transient pulses

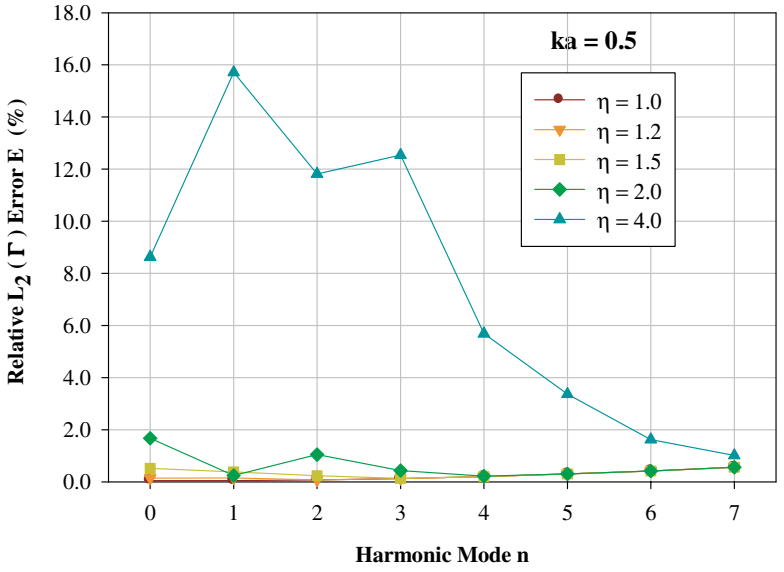

Fig. 12. Relative L_2 error E for elliptical ($s_M = 6a$) and circular boundaries; $ka = 0.5$; various harmonic modes.

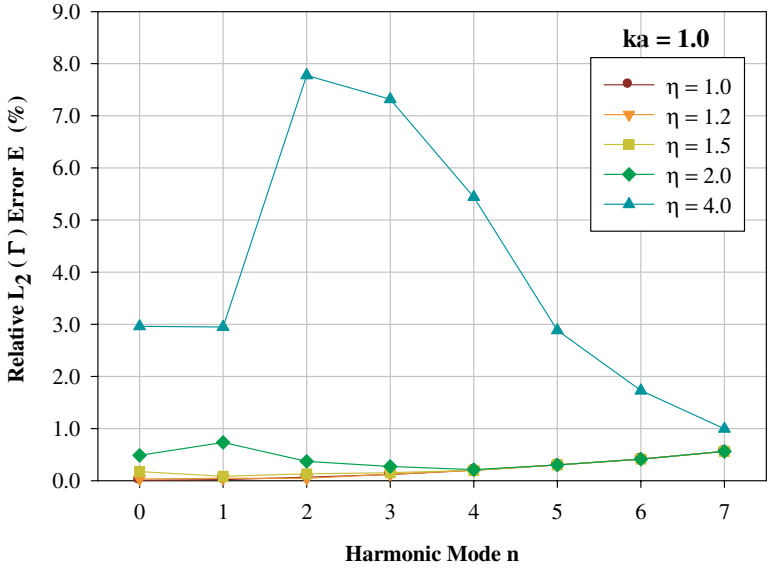

Fig. 13. Relative L_2 error E for elliptical ($s_M = 6a$) and circular boundaries; $ka = 1.0$; various harmonic modes.

exhibiting strong zero-frequency components (e.g. [45]) that have shown that the second-order circular boundaries perform surprisingly well even at near-static cases ($ka \simeq 0.05$), provided that they are not used extremely close to the scatterer or as on-surface conditions. Secondly, the closeness of the boundary to the scatterer is also responsible for larger errors on the absorbing boundary—tantamount to reflections. Due to the elongated boundary shape at high η ratios, the multiple reflections tend to form focusing regions where

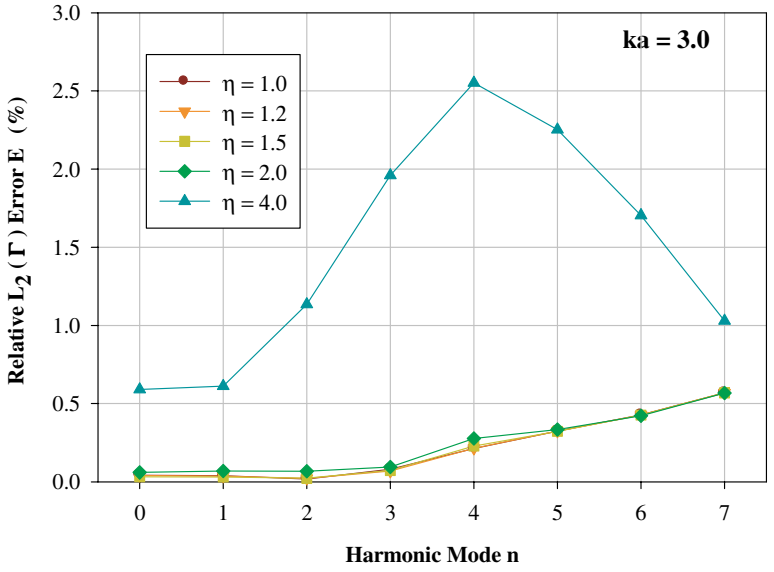

Fig. 14. Relative L_2 error E for elliptical ($s_M = 6a$) and circular boundaries; $ka = 3.0$; various harmonic modes.

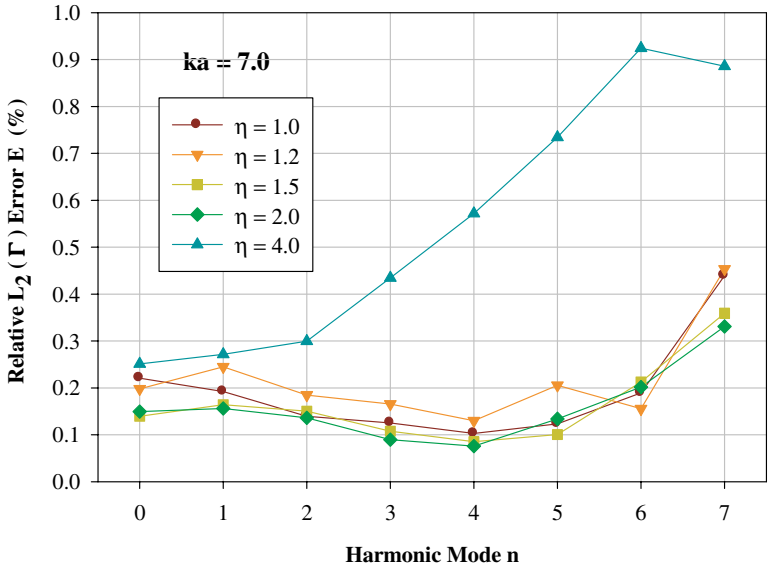

Fig. 15. Relative L_2 error E for elliptical ($s_M = 6a$) and circular boundaries; $ka = 7.0$; various harmonic modes.

the errors are exacerbated, thus further polluting the solution on the scatterer's boundary. As it appears from the numerical results, despite this shortcoming at the low frequency-small distance regime, in all cases there are ellipses (various η ratios) for which the accuracy is comparable to the circular boundaries, thus realizing moderate to significant computational savings. In the higher frequency regime (e.g. Fig. 15), clearly, any of the tested elliptical configurations exhibit comparable performance to the circular boundary.

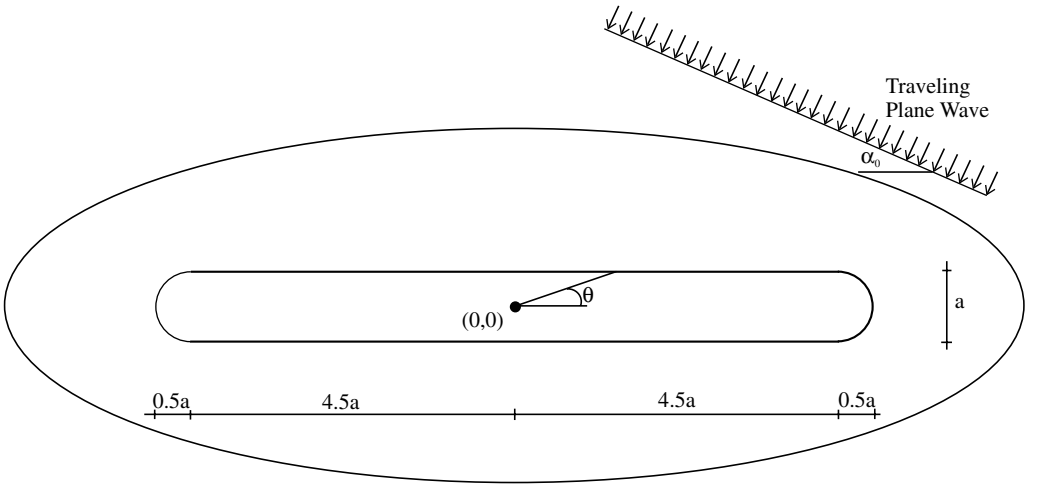

Fig. 16. Geometry of cigar-shaped rigid scatterer; length-to-width ratio ≃10:1.

Table 2
Relative $L_2(\Gamma)$ errors (E) in percent for harmonic mode $n = 5$

ka	$\eta = 1.0$	$\eta = 1.2$	$\eta = 1.5$	$\eta = 2.0$	$\eta = 4.0$
$s_M = 6a$					
0.5	0.3009	0.3009	0.3010	0.3025	3.3592
1.0	0.3012	0.3012	0.3011	0.3008	2.8841
3.0	0.3244	0.3242	0.3228	0.3338	2.2534
7.0	0.1231	0.2053	0.1005	0.1338	0.7341
$s_M = 3a$					
0.5	0.3016	0.3053	0.4084	2.6062	N/A
1.0	0.2988	0.2977	0.3765	2.4018	N/A
3.0	0.3243	0.3003	0.6345	2.1412	N/A
7.0	0.2606	0.2148	0.2755	0.7329	N/A

Moreover, as the driving frequency increases and/or the harmonic mode increases, thus giving rise to wave fronts that depart significantly from a purely radial form ($n = 0$), the elliptical boundaries display excellent agreement with the exact solution at substantial savings compared to the circular boundaries. Notice that, as shown in Table 1 the elliptical boundaries require anywhere between 82% and 22% of the degrees-of-freedom of the circular boundaries. For example, in Table 2 we summarize the errors for a higher mode ($n = 5$) and various frequencies and ellipse ratios. Clearly, for the same level of accuracy, i.e., for the same error E, in most cases shown in Table 2, the elliptical boundaries perform as well as the circular boundaries. The computational savings however are substantial: for $\eta = 2$ one needs only 47% of the degrees-of-freedom alloted to the circular case for comparable accuracy.

4.2. Scattering problems—frequency-domain

The potential computational savings, as indicated already by the preceding simple radiation test cases, are expected to be greater in the presence of elongated scatterers, where an elliptical boundary can better

circumscribe the insonified obstacle. To this end, we discuss the performance of a cigar-shaped scatterer (Fig. 16) subjected to an incoming plane wave impinging obliquely on the scatterer (angle of incidence α_0).

In this case there is no exact solution to compare against. We thus measure the relative error against a reference solution, which we obtain as follows: we first place a circular boundary endowed with the second-order condition, at a distance of $R = 9a$, using a mesh with $h = 0.025a$. We compute the trace of the scattered pressure on the boundary of the cigar-shaped scatterer and treat it as the reference solution. Different ellipses with $s_M = 6a$ and various η ratios ranging from 1 (circle) to 4 were used as boundaries. Figs. 17 and 18 depict the real and imaginary part, respectively, of the trace of the normalized scattered pressure on the boundary of the cigar-shaped scatterer against the polar angle θ for an incident wave impinging at an angle $\alpha_0 = 60°$ and for a relatively low frequency $ka = 1$. Clearly, the depicted agreement between the reference solution and the various ellipses is quite satisfactory; Table 3 reports the degrees-of-

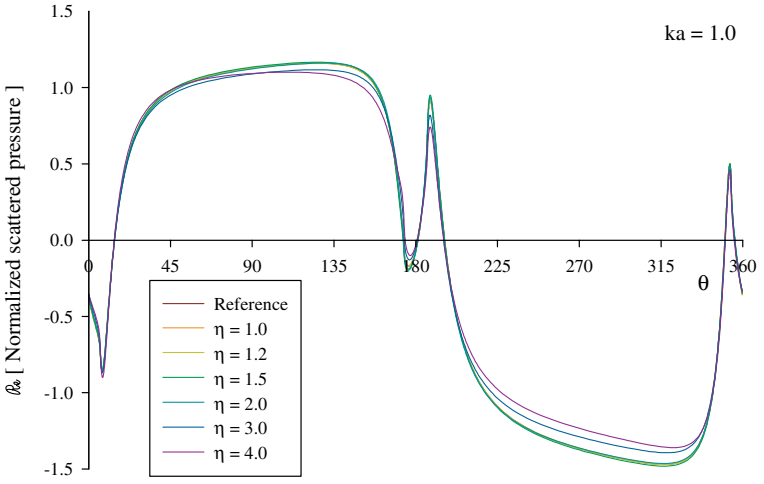

Fig. 17. Real part of normalized scattered pressure on the scatterer for $ka = 1$.

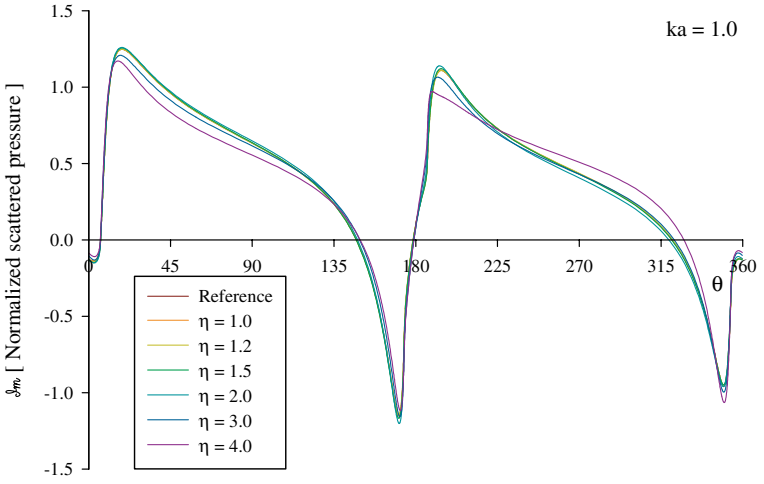

Fig. 18. Imaginary part of normalized scattered pressure on the scatterer for $ka = 1$.

Table 3
Total degrees-of-freedom per configuration (cigar-shaped scatterer); all ellipses with $s_M = 6a$; reference solution with circular boundary at 9a

Semi-axes ratio $\eta = s_M/s_m$	Total DOF
4.0	32,252
3.0	48,416
2.0	80,760
1.5	114,076
1.2	147,796
1.0	182,384
Reference	423,180

freedom used in each of the shown cases. Notice again that, for example, for $\eta = 3$ one needs less than one-fourth of the degrees-of-freedom of a circular boundary for comparable accuracy.

Similarly, Fig. 19 depict the distribution of the amplitude of the scattered pressure within the entire computational domain for a higher dimensionless frequency of $ka = 15$. Specifically, Fig. 19a depicts the projection of the reference solution (obtained with a boundary at 9a) onto a circular domain with radius 6a in order to ease the comparison with the elliptical domains shown in Fig. 19b–d. Again, the agreement (in the visual norm) is quite satisfactory.

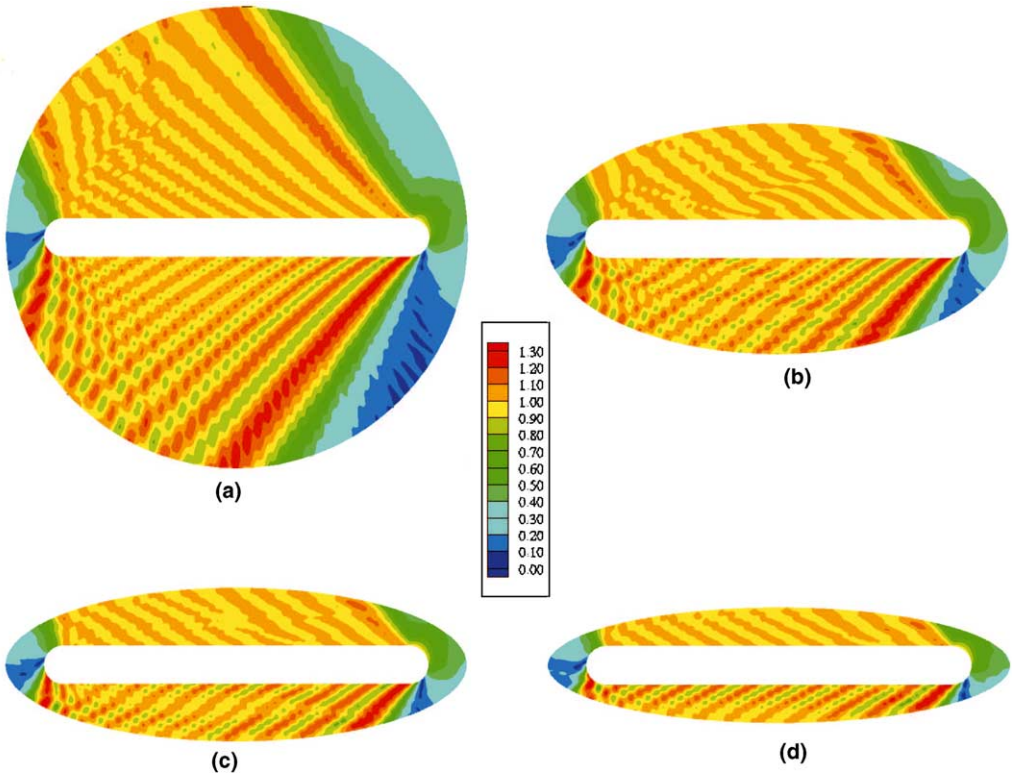

Fig. 19. Distribution of normalized scattered pressure amplitude due to an incident plane wave; $ka = 15$; reference solution and ellipse ratios $\eta = 1, 2, 3, 4$.

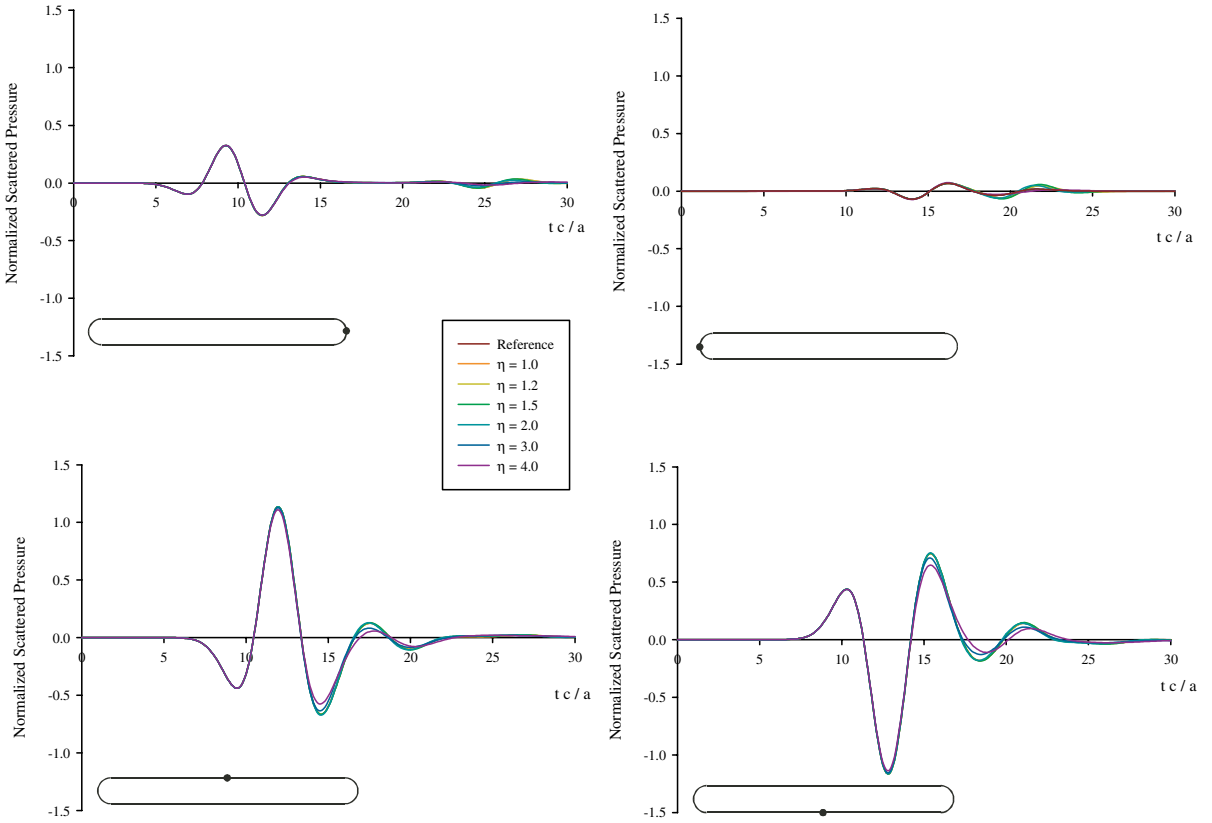

Fig. 20. Normalized scattered pressure traces; transient response to a traveling plane wave (Ricker pulse).

4.3. Scattering problems—time-domain

To illustrate the applicability of the absorbing elements to time-domain applications, Fig. 20 pertain to a direct time-domain solution of (42) for the scattered pressure field due to the insonification of the cigar-shaped scatterer by a traveling plane wave at four points denoted by the solid dots on the cigar-shaped schematic. To formally define the corresponding IBVP problem we set the normal derivative of the scattered pressure equal to the negative of the normal derivative of the incident pressure on the scatterer. We use the implicit trapezoidal rule to integrate in time the semi-discrete form (42) with a time-step $\Delta tc/a = 0.1$. Finally, the time signal for the plane wave is given by a modified Ricker pulse (see Appendix A). [7] The reference solution against which the traces in Fig. 20 are compared was obtained by placing a circular boundary endowed with the second-order condition at a radial distance of 9a.

Fig. 21 depicts a pointwise error measure $e(t)$, whereas Fig. 22 depict both the absolute and relative L_2-norm errors $E^a(t)$ and $E(t)$, defined, respectively, as:

$$e(t) = p_{\text{ex}}(\boldsymbol{x}, t) - p_{\text{app}}(\boldsymbol{x}, t), \tag{46a}$$

[7] The Ricker pulse (Fig. 23a), often used in seismology, is such that its Fourier transform has well-defined user-controllable spectrum support that is characterized by a peak central frequency ω_r (Fig. 23b). For the cases shown in Fig. 20 we used $\omega_r a/c = 1$.

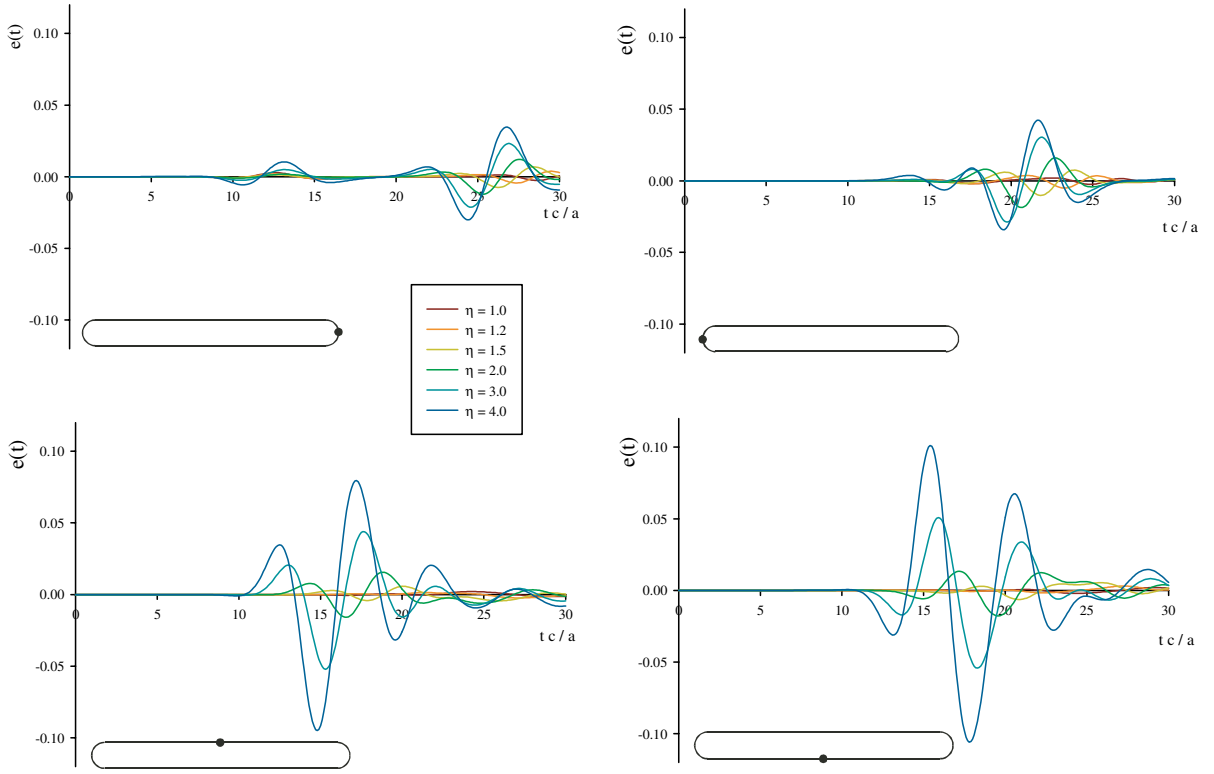

Fig. 21. Pointwise error $e(t)$; transient response to a traveling plane wave (Ricker pulse).

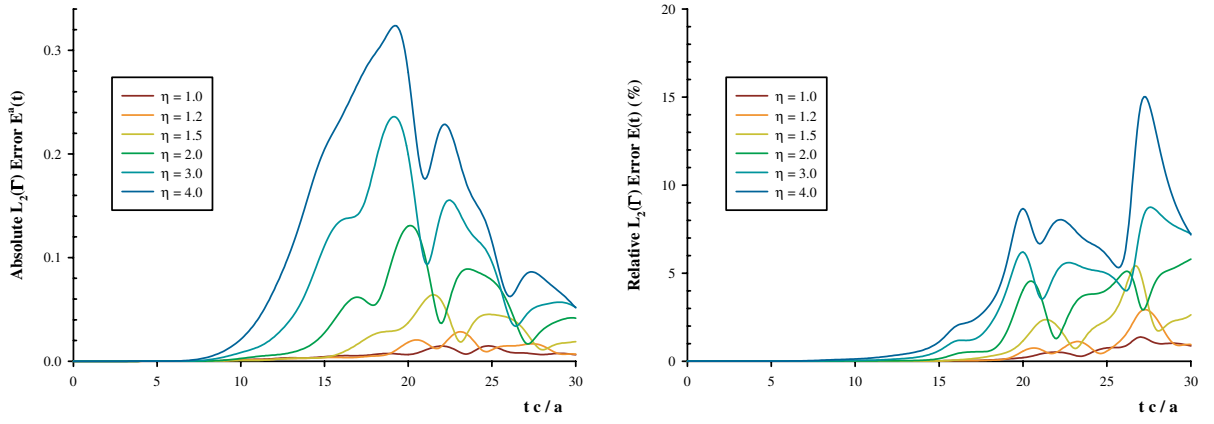

Fig. 22. L_2-norm absolute (left) and relative (right) errors; transient response to a traveling plane wave (Ricker pulse).

with $\boldsymbol{x}$ one of the four characteristic points as per the inset in Fig. 21, and

$$E^a(t) = \left[\int_\Gamma \left[p_{\text{ex}}(\boldsymbol{x}, t) - p_{\text{app}}(\boldsymbol{x}, t) \right]^2 \mathrm{d}\Gamma \right]^{1/2}, \quad \boldsymbol{x} \in \Gamma, \tag{46b}$$

$$E(t) = \frac{E^a(t)}{\left[\int_\Gamma p_{\text{ex}}^2(\boldsymbol{x},t)\mathrm{d}\Gamma\right]^{1/2}}, \quad \boldsymbol{x} \in \Gamma. \tag{46c}$$

Overall, the same qualitative behavior and features already identified in the frequency-domain characterize the response in time as well. Specifically, from Fig. 20 the agreement between all elliptical configurations and the reference solution appears quite satisfactory. However, as it is evident from Figs. 21 and 22 the higher ellipse ratios result in higher errors. Still, the agreement between the reference solution and, e.g., the $\eta = 1.5$ elliptically-shaped boundary is excellent (higher relative errors past time 20–25 in Fig. 22 are due to very low response amplitudes).

5. Conclusions

In this paper, we presented results pertaining to second- and third-order absorbing boundary conditions prescribed on elliptically-shaped boundaries for the numerical simulation of scalar waves in either the time- or the frequency-domains. The local wave absorption properties of the condition depend on the curvature of the truncation boundary, and terms accounting for the curvature variations appear explicitly in the developed conditions. We have shown the equivalence of the conditions, upon discretization under a Galerkin scheme, to simple wave absorbing finite elements fully described by symmetric frequency-independent element matrices. We have derived the element matrices for both second- and third-order conditions; the elements can be readily implemented to any general-purpose finite element code.

Based on the obtained numerical results we conclude that significant computational savings are attainable by the use of the proposed elliptically-shaped boundaries endowed with second- or third-order conditions compared to the corresponding circular boundaries for a wide range of frequencies. The savings, measured in the number of unknowns in the resulting algebraic system, are of the order of four to five times over the circular boundaries. We have observed performance deterioration at the low end of the spectrum and in particular in cases where the boundaries are placed at a distance that corresponds to a tiny fraction (in the hundredths) of the dominant wavelength. We thus recommend their use, even at high ellipse ratios, provided that the boundaries are placed at distances from the surface of the scatterers that do not fall below 0.1 of the dominant wavelength.

Appendix A

A.1. Proof of (6a)

We prove (6a), i.e., we show that

$$\hat{p}(\boldsymbol{x},s) = \int_0^\infty \mathrm{e}^{-st}\widehat{P}(\boldsymbol{x},s;t)\mathrm{d}t, \quad \boldsymbol{x} \in \overline{\Omega}^+, \tag{A.1}$$

is indeed a solution to the following initial and boundary value problem for the exterior wave equation:

$$\ddot{p}(\boldsymbol{x},t) = c^2\Delta p(\boldsymbol{x},t), \quad \boldsymbol{x} \in \overline{\Omega}^+, \quad t > 0, \tag{A.2a}$$

$$p(\boldsymbol{x},t) = \widehat{P}(\boldsymbol{x},s;t), \quad \boldsymbol{x} \in \Gamma_a, \quad t > 0, \tag{A.2b}$$

$$p(\boldsymbol{x},0) = 0, \quad \dot{p}(\boldsymbol{x},0) = 0, \quad \boldsymbol{x} \in \overline{\Omega}^+. \tag{A.2c}$$

To this end, we consider the same problem (A.2) with, however, a unit step function as the Dirichlet datum on Γ_a. Accordingly, let $q(\boldsymbol{x},t)$ be the solution to

$$\ddot{q}(\boldsymbol{x},t) = c^2\Delta q(\boldsymbol{x},t), \quad \boldsymbol{x}\in\overline{\Omega}^+, \quad t>0, \tag{A.3a}$$

$$q(\boldsymbol{x},t) = 1, \quad \boldsymbol{x}\in\Gamma_a, \quad t>0, \tag{A.3b}$$

$$q(\boldsymbol{x},0) = 0, \quad \dot{q}(\boldsymbol{x},0) = 0, \quad \boldsymbol{x}\in\overline{\Omega}^+. \tag{A.3c}$$

Then, by direct application of Duhamel's principle [55], one obtains

$$[p(\boldsymbol{x},t)]_{\boldsymbol{x}\in\overline{\Omega}^+} = [q(\boldsymbol{x},0)]_{\boldsymbol{x}\in\overline{\Omega}^+}[\widehat{P}(\boldsymbol{x},s;t)]_{\boldsymbol{x}\in\Gamma_a} + \int_0^t [\widehat{P}(\boldsymbol{x},s;t)]_{\boldsymbol{x}\in\Gamma_a}\left[\frac{\partial q(\boldsymbol{x},t-\tau)}{\partial t}\right]_{\boldsymbol{x}\in\overline{\Omega}^+}\mathrm{d}\tau. \tag{A.4}$$

Application of the Laplace transform on (A.4), while taking into account the initial conditions (A.3c), leads to

$$\begin{aligned}\hat{p}(\boldsymbol{x},s) &= s[\hat{q}(\boldsymbol{x},s)]_{\boldsymbol{x}\in\overline{\Omega}^+}\int_0^t \mathrm{e}^{-st}[\widehat{P}(\boldsymbol{x},s;t)]_{\boldsymbol{x}\in\Gamma_a}\mathrm{d}t = \int_0^t \mathrm{e}^{-st}\left[s[\hat{q}(\boldsymbol{x},s)]_{\boldsymbol{x}\in\overline{\Omega}^+}[\widehat{P}(\boldsymbol{x},s;t)]_{\boldsymbol{x}\in\Gamma_a}\right]\mathrm{d}t \\ &\equiv \int_0^t \mathrm{e}^{-st}[\widehat{P}(\boldsymbol{x},s;t)]_{\boldsymbol{x}\in\overline{\Omega}^+}\mathrm{d}t,\end{aligned} \tag{A.5}$$

where we defined

$$[\widehat{P}(\boldsymbol{x},s;t)]_{\boldsymbol{x}\in\overline{\Omega}^+} = s[\hat{q}(\boldsymbol{x},s)]_{\boldsymbol{x}\in\overline{\Omega}^+}[\widehat{P}(\boldsymbol{x},s;t)]_{\boldsymbol{x}\in\Gamma_a}. \tag{A.6}$$

Notice that (A.6) holds also for $\boldsymbol{x}$ on Γ_a, since, by virtue of (A.3b), $\hat{q}(\boldsymbol{x},s) = 1/s$ on Γ_a. Eq. (A.5) completes the proof. Alternatively, it can also be seen, by inspection, that (A.1) (or (8a)) satisfies the field equation (4) and the boundary condition (5b).

A.2. Metrics of the Fermi-type coordinate system

We derive next expressions for the gradient, Laplacian, and normal derivative for the coordinate system defined in (12). Accordingly, the components g_{ij} of the Euclidean metric tensor that characterizes the transformation from a cartesian coordinate system to the coordinate system defined by (12), are given as (subscripts denote partial derivatives)

$$g_{11} = \boldsymbol{R}_\lambda\cdot\boldsymbol{R}_\lambda = \boldsymbol{X}_\lambda\cdot\boldsymbol{X}_\lambda + 2\xi\boldsymbol{X}_\lambda\cdot\boldsymbol{v}_\lambda + \xi^2\boldsymbol{v}_\lambda\cdot\boldsymbol{v}_\lambda, \tag{A.7a}$$

$$g_{22} = \boldsymbol{R}_\xi\cdot\boldsymbol{R}_\xi = \boldsymbol{v}\cdot\boldsymbol{v} = 1, \tag{A.7b}$$

$$g_{12} = g_{21} = \boldsymbol{R}_\lambda\cdot\boldsymbol{R}_\xi = (\boldsymbol{X}_\lambda + \xi\boldsymbol{v}_\lambda)\cdot\boldsymbol{v}. \tag{A.7c}$$

Moreover, the tangent unit vector $\boldsymbol{t}$, the unit normal $\boldsymbol{v}$ and the curvature κ of a plane curve such as Γ_a are related as follows:

$$\boldsymbol{t} \equiv \boldsymbol{X}_\lambda, \tag{A.8a}$$

$$\boldsymbol{v}_\lambda = -\kappa\boldsymbol{t}. \tag{A.8b}$$

By virtue of (A.8), (A.7a) and (A.7c) become

$$g_{11} = 1 - 2\xi\kappa + \xi^2\kappa^2 = (1-\xi\kappa)^2 \equiv Q^2, \tag{A.9a}$$

$$g_{12} = g_{21} = 0, \tag{A.9b}$$

while the determinant of the metric tensor is

$$g = g_{11}g_{22} - g_{12}^2 = Q^2. \tag{A.10}$$

It can be further shown that for any scalar field Φ, one has

$$\nabla\Phi = \frac{g_{22}}{g}\Phi_\lambda \boldsymbol{R}_\lambda + \frac{g_{11}}{g}\Phi_\xi \boldsymbol{R}_\xi = \frac{1}{Q^2}\Phi_\lambda \boldsymbol{R}_\lambda + \Phi_\xi \boldsymbol{R}_\xi, \tag{A.11a}$$

$$\Delta\Phi = \frac{1}{\sqrt{g}}\left[\left(\frac{g_{22}}{\sqrt{g}}\Phi_\lambda\right)_\lambda + \left(\frac{g_{11}}{\sqrt{g}}\Phi_\xi\right)_\xi\right] = \frac{1}{Q}\left[\left(\frac{1}{Q}\Phi_\lambda\right)_\lambda + (Q\Phi_\xi)_\xi\right]. \tag{A.11b}$$

By virtue of (A.11a) the following also holds true:

$$\Phi_v = \nabla\Phi \cdot \boldsymbol{v} = \Phi_\xi. \tag{A.11c}$$

Finally, from (A.9a) one also has

$$Q_\lambda = -\xi\kappa_\lambda, \tag{A.12a}$$

$$Q_{\lambda\lambda} = -\xi\kappa_{\lambda\lambda}, \tag{A.12b}$$

$$Q_\xi = -\kappa, \tag{A.12c}$$

$$Q_{\xi\xi} = 0, \tag{A.12d}$$

$$Q_{\lambda\xi} = -\kappa_\lambda. \tag{A.12e}$$

A.3. A proof on the ellipse's curvature

We prove that

$$3\kappa^3 + \kappa_{\lambda\lambda} < 0, \tag{A.13}$$

for all ellipses, as we claimed in Section 3.2.1. Let s_M, s_m denote the major and minor semi-axes of an ellipse respectively, and $\eta = \frac{s_M}{s_m}$ the semi-axes ratio ($\eta \geqslant 1$); then any point (x, y) on the ellipse is defined by the parametric representation $x = s_M \cos\theta$ and $y = s_m \sin\theta$. Moreover:

$$\mathrm{d}\lambda = j\mathrm{d}\theta \quad \text{with } j = \sqrt{s_M^2 \sin^2\theta + s_m^2 \cos^2\theta} = s_m\sqrt{\eta^2 \sin^2\theta + \cos^2\theta}, \tag{A.14a}$$

$$\kappa = -\frac{s_M s_m}{j^3} = -\frac{\eta}{s_m(\eta^2 \sin^2\theta + \cos^2\theta)^{3/2}}, \tag{A.14b}$$

$$\kappa_{\lambda\lambda} = \frac{3\eta(\eta^2-1)[4(1-\eta^2)\sin^2\theta\cos^2\theta + \cos^2\theta - \eta^2\sin^2\theta]}{s_m^3(\eta^2\sin^2\theta + \cos^2\theta)^{9/2}}. \tag{A.14c}$$

Then

$$3\kappa^3 + \kappa_{\lambda\lambda} = \frac{12 s_m^6 \eta(1-\eta^2)^2}{j^9}(\sin^2\theta - r_1)(\sin^2\theta - r_2) \tag{A.15}$$

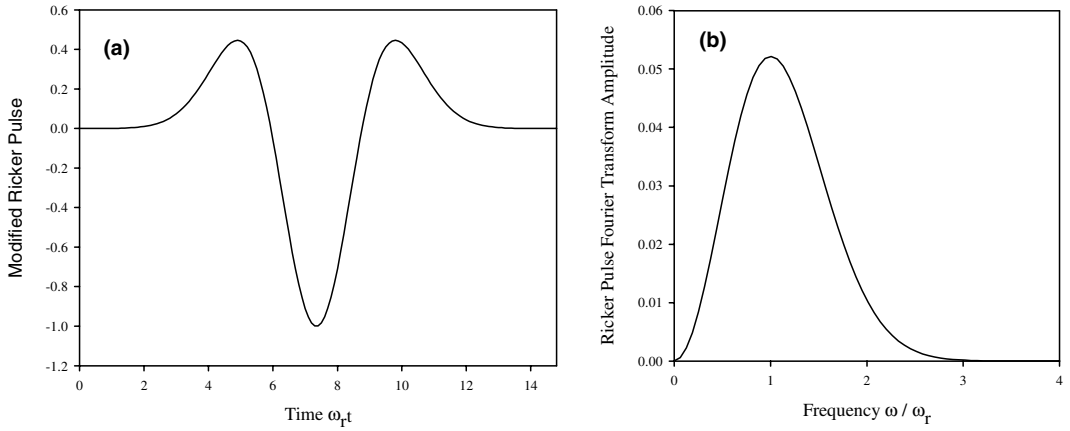

Fig. 23. (a) Finite-duration modified Ricker pulse; (b) Amplitude of Fourier Transform of (a).

with

$$r_{1,2} = \frac{-5\eta^2 + 3 \pm \sqrt{25\eta^4 - 30\eta^2 + 25}}{8(1-\eta^2)}. \tag{A.16}$$

It can be easily seen now that the first two terms in parentheses in (A.15) are always positive, whereas the last term is always negative, for all values of the semi-axes ratio $\eta \geqslant 1$, and thus (A.13) holds.

A.4. Modified Ricker pulse

In the numerical results Section 4 we introduced a modified Ricker pulse as the time signal for the time-domain simulations. The pulse is defined by

$$f_r(z) = \frac{(0.25u^2 - 0.5)\mathrm{e}^{-0.25u^2} - 13\mathrm{e}^{-13.5}}{0.5 + 13\mathrm{e}^{-13.5}} \quad \text{with } 0 \leqslant z \leqslant \frac{6\sqrt{6}}{\omega_r}, \tag{A.17a}$$

where

$$u = \omega_r z - 3\sqrt{6} \tag{A.17b}$$

with ω_r denoting the characteristic frequency of the Ricker pulse. Fig. 23 depicts the Ricker signal and the amplitude of its Fourier transform.

References

[1] I. Harari, T.J.R. Hughes, A cost comparison of boundary element and finite element methods for problems in time-harmonic acoustics, Comput. Methods Appl. Mech. Engrg. 97 (1992) 77–102.
[2] R.D. Mindlin, H.H. Bleich, Response of an elastic cylindrical shell to a transverse, step shock wave, ASME J. Appl. Mech. 20 (1953) 189–195.
[3] E. Kausel, J.L. Tassoulas, Transmitting boundaries : a closed-form comparison, Bull. Seismol. Soc. Am. 71 (1981) 143–159.
[4] J.P. Wolf, A comparison of time-domain transmitting boundaries, Earthq. Engrg. Str. Dyn. 14 (1986) 655–673.
[5] E. Kausel, Local transmitting boundaries, ASCE J. Engrg. Mech. 114 (6) (1988) 1011–1027.
[6] D. Givoli, Non-reflecting boundary conditions: A review, J. Comput. Phys. 94 (1) (1991) 1–29.

[7] S.V. Tsynkov, Numerical solution of problems on unbounded domains. A review, Appl. Numer. Math. 27 (1998) 465–532.
[8] B. Engquist, A. Majda, Absorbing boundary conditions for the numerical simulation of waves, Math. Comput. 31 (1977) 629–651.
[9] B. Engquist, A. Majda, Radiation boundary conditions for acoustic and elastic wave calculations, Commun. Pure Appl. Math. 32 (1979) 313–357.
[10] A. Bayliss, E. Turkel, Radiation boundary conditions for wave-like equations, Commun. Pure Appl. Math. 33 (1980) 707–725.
[11] A. Bayliss, E. Turkel, Far field boundary conditions for compressible flows, J. Comput. Phys. 48 (1982) 182–199.
[12] A. Bayliss, M. Gunzburger, E. Turkel, Boundary conditions for the numerical solution of elliptic equations in exterior regions, SIAM J. Appl. Math. 42 (2) (1982) 430–451.
[13] J. Assaad, J.-N. Decarpigny, C. Bruneel, R. Bossut, B. Hamonic, Application of the finite element method to two-dimensional radiation problems, J. Acoust. Soc. Am. 94 (1) (1993) 562–573.
[14] R. Bossut, J.-N. Decarpigny, Finite element modeling of radiating structures using dipolar damping elements, J. Acoust. Soc. Am. 86 (4) (1989) 1234–1244.
[15] N.N. Abboud, P.M. Pinsky, Finite element solution and dispersion analysis for the transient structural acoustics problem, Appl. Mech. Rev. 43 (5) (1990) S381–S388, Pt. 2.
[16] P.M. Pinsky, N.N. Abboud, Transient finite element analysis of the exterior structural acoustics problem, ASME J. Vibrat. Acoust. 112 (1990) 245–256.
[17] P.M. Pinsky, N.N. Abboud, Finite element solution of the transient exterior structural acoustics problem based on the use of radially asymptotic boundary operators, Comput. Methods Appl. Mech. Engrg. 85 (1991) 311–348.
[18] R.C. MacCamy, S.P. Marin, A finite element method for exterior interface problems, Int. J. Math. Math. Sci. 3 (1980) 311–350.
[19] D. Givoli, J.B. Keller, A finite element method for large domains, Comput. Methods Appl. Mech. Engrg. 76 (1989) 41–66.
[20] J.B. Keller, D. Givoli, Exact non-reflecting boundary conditions, J. Comput. Phys. 82 (1989) 172–192.
[21] I. Harari, T.J.R. Hughes, Design and analysis of finite element methods for the Helmholtz equation in exterior domains, Appl. Mech. Rev. 43 (5) (1990) S366–S373, Pt. 2.
[22] I. Harari, T.J.R. Hughes, Finite element methods for the Helmholtz equation in an exterior domain: Model problems, Comput. Methods Appl. Mech. Engrg. 87 (1991) 59–96.
[23] I. Harari, T.J.R. Hughes, Galerkin/least-squares finite element methods for the reduced wave equation with non-reflecting boundary conditions in unbounded domains, Comput. Methods Appl. Mech. Engrg. 98 (1992) 411–454.
[24] C. Lubich, A. Schädle, Fast convolution for nonreflecting boundary conditions, SIAM J. Sci. Comput. 24 (1) (2002) 161–182.
[25] B. Alpert, L. Greengard, T. Hagstrom, Rapid evaluation of nonreflecting boundary kernels for time-domain wave propagation, SIAM J. Numer. Anal. 37 (4) (2000) 1138–1164.
[26] P. Bettess, O.C. Zienkiewicz, Diffraction and refraction of surface waves using finite and infinite elements, Int.J. Numer. Methods Engrg. 11 (1977) 1271–1290.
[27] P. Bettess, Infinite elements, Int. J. Numer. Methods Engrg. 11 (1977) 53–64.
[28] D.S. Burnett, A three-dimensional acoustic infinite element based on a prolate spheroidal multipole expansion, J. Acoust. Soc. Am 96 (5) (1994) 2798–2816.
[29] D.S. Burnett, R.L. Holford, Prolate and oblate spheroidal acoustic infinite elements, Comput. Methods Appl. Mech. Engrg. 158 (1998) 117–142.
[30] D.S. Burnett, R.L. Holford, An ellipsoidal acoustic infinite element, Comput. Methods Appl. Mech. Engrg. 164 (1998) 49–76.
[31] J. Astley, Transient wave envelope elements for wave problems, J. Sound Vibrat. 192 (1996) 245–261.
[32] J. Astley, Transient spheroidal elements for unbounded wave problems, Comput. Methods Appl. Mech. Engrg. 164 (1998) 3–15.
[33] J.P. Bérenger, A perfectly matched layer for the absorption of electromagnetic waves, J. Comput. Phys. 41 (1994) 115–135.
[34] Q. Qi, T.L. Geers, Evaluation of the perfectly matched layer for computational acoustics, J. Comput. Phys. 139 (1) (1998) 166–183.
[35] S. Abarbanel, D. Gottlieb, A mathematical analysis of the PML method, J. Comput. Phys. 134 (1997) 357–363.
[36] G.A. Kriegsmann, A. Taflove, K.R. Umashankar, A new formulation of electromagnetic wave scattering using an on-surface radiation boundary condition approach, IEEE Trans. Antennas Propagat. AP-35 (2) (1987) 153–160.
[37] D.S. Jones, An approximate boundary condition in acoustics, J. Sound. Vibrat. 121 (1) (1988) 37–45.
[38] A. Khebir, O. Ramahi, R. Mittra, An efficient partial differential equation technique for solving the problem of scattering by objects of arbitrary shape, Microwave Opt. Tech. Lett. 2 (1989) 229–233.
[39] C.F. Lee, R.T. Shin, J.A. Kong, B.J. McCartin, Absorbing boundary conditions on circular and elliptical boundaries, J. Electromagn. Waves Applicat. 4 (10) (1990) 945–962.
[40] Y. Li, Z.J. Cendes, Modal expansion absorbing boundary conditions for two-dimensional electromagnetic scattering, IEEE Trans. Magn. 29 (1993) 1835–1838.
[41] B. Stupfel, Absorbing boundary conditions on arbitrary boundaries for the scalar and wave equations, IEEE Trans. Antennas Propagat. 42 (6) (1994) 773–780.
[42] M.J. Grote, J.B. Keller, On nonreflecting boundary conditions, J. Comput. Phys. 122 (1995) 231–243.

[43] X. Antoine, H. Barucq, A. Bendali, Bayliss–Turkel-like radiation conditions on surfaces of arbitrary shape, J. Math. Anal. Applicat. 229 (1999) 184–211.
[44] A. Barry, J. Bielak, R.C. MacCamy, On absorbing boundary conditions for wave propagation, J. Comput. Phys. 79 (1988) 449–468.
[45] L.F. Kallivokas, J. Bielak, R.C. MacCamy, Symmetric local absorbing boundaries in time and space, ASCE J. Engrg. Mech. 117 (9) (1991) 2027–2048.
[46] L.F. Kallivokas, Absorbing boundary conditions and finite elements for transient and harmonic steady-state acoustic fluid-structure interaction, Thesis presented to Carnegie Mellon University in partial fulfillment of the requirements for the degree of Doctor of Philosophy, Pittsburgh, 1995.
[47] L.F. Kallivokas, J. Bielak, R.C. MacCamy, Absorbing boundary conditions of arbitrary shape for the three-dimensional wave equation, in: Proceedings of the IUTAM Symposium on Computational Methods for Unbounded Domains, Kluwer Academic Publishers, Boulder, CO, July 1997, pp. 221–228.
[48] L.F. Kallivokas, J. Bielak, R.C. MacCamy, A simple impedance-infinite element for the finite element solution of the three-dimensional wave equation in unbounded domains, Comput. Methods Appl. Mech. Engrg. 147 (1997) 235–262.
[49] R. Djellouli, C. Farhat, A. Macedo, R. Tezaur, Finite element solution of two-dimensional acoustic scattering problems using arbitrarily shaped convex artificial boundaries, J. Comput. Acoust. 8 (1) (2000) 81–99.
[50] S.K. Bhattacharyya, S. Sathyapal, C.P. Vendhan, Absorbing boundary condition on elliptic boundary for the finite element analysis of water wave diffraction by large elongated bodies, Int. J. Numer. Methods Fluids 37 (2001) 249–277.
[51] D.B. Meade, G.W. Slade, A.F. Peterson, K.J. Webb, Comparison of local radiation boundary conditions for the scalar Helmholtz equation with general boundary shape, IEEE Trans. Antennas Propagat. 43 (1995) 1–5.
[52] B. Lichtenberg, K.J. Webb, D.B. Meade, A.F. Peterson, Comparison of two-dimensional conformal local radiation boundary conditions, Electromagnetics 16 (1996) 359–384.
[53] L.F. Kallivokas, J. Bielak, Time-domain analysis of transient structural acoustics problems based on the finite element method and a novel absorbing boundary element, J. Acoust. Soc. Am. 94 (6) (1993) 3480–3492.
[54] L.F. Kallivokas, J. Bielak, An element for the analysis of transient exterior fluid–structure interaction problems using the FEM, Finite Elem. Anal. Design 15 (1993) 69–81.
[55] R. Courant, D. Hilbert, in: Methods of Mathematical Physics, Vol. II Partial Differential Equations, Wiley Classics Edition, Interscience Publishers, New York, NY, 1989.
[56] T. Hagstrom, and S.I. Hariharan, Progressive wave expansions and open boundary problems, In: B. Engquist, G.A. Kriegsmann (Eds.), Computational Wave Propagation, IMA Volumes in Mathematics and its Applications, vol. 86, 1997, pp. 23–43.
[57] T. Hagstrom, S.I. Hariharan, A formulation of asymptotic and exact boundary conditions using local operators, Appl. Numer. Math. 27 (1998) 403–416.
[58] D. Givoli, High-order non-reflecting boundary conditions without high-order derivatives, J. Computat. Phys. 170 (2001) 849–870.
[59] D. Givoli, B. Neta, High-order non-reflecting boundary scheme for time-dependent waves, J. Computat. Phys. 186 (2003) 24–46.